12-26-2025

Endothelial TLR4 signaling drives tissue inflammation, Claudin-5 internalization, and vascular barrier breakdown in a mouse model of neonatal meningitis

Philip V. Seegren[1,2], Amir Rattner[1,2], Philip M. Smallwood[1,2], Jeremy Nathans[1,2,3,4]

[1]Department of Molecular Biology and Genetics, Johns Hopkins University School of Medicine, Baltimore, United States
[2]Howard Hughes Medical Institute, Johns Hopkins University School of Medicine, Baltimore, United States
[3]Department of Neuroscience, Johns Hopkins University School of Medicine, Baltimore, United States
[4]Department of Ophthalmology, Johns Hopkins University School of Medicine, Baltimore, United States

Number of pages: 41
Number of figures: 6
Number of tables: 0
Number of supplementary figures: 9
Number of supplementary files: 2

Address for editorial correspondence:
Dr. Jeremy Nathans
805 PCTB
725 North Wolfe Street
Johns Hopkins University School of Medicine
Baltimore, MD 21205
tel: 410 955 4679
fax: 410 614 0827
email: jnathans@jhmi.edu

Abstract

Neonatal bacterial meningitis is a leading cause of infant morbidity and mortality, yet the molecular and cellular basis of the leptomeningeal response to infection remains poorly defined. Here, we study a mouse model of neonatal *E. coli* meningitis, combining cell-type specific gene knockouts, leptomeningeal single-nucleus RNA sequencing, and endothelial cell culture to explore the role of Toll-like receptor 4 (TLR4) signaling in the host response to infection. Endothelial-specific deletion of *Tlr4* dramatically reduced the inflammatory response in all leptomeningeal cell types and abrogated the infection-associated increase in vascular permeability. In a brain endothelial cell line (bEnd.3 cells), exposure to *E. coli* triggered TLR4-dependent NF-κB activation, selective internalization of Claudin-5, and increased monolayer permeability, responses that were eliminated by *Tlr4* knockout. RNA-seq showed that endothelial TLR4 controls an NF-κB–driven transcriptional program that orchestrates the leptomeningeal response to infection. These findings reframe the host response in neonatal Gram-negative bacterial meningitis as an endothelial-centric process.

Introduction

Bacterial meningitis is a major global health challenge, causing ~250,000 deaths annually (Brouwer, 2010; GBD 2016 Neurology Collaborators, 2019). Among neonates, Group B Streptococcus (*Streptococcus agalactiae*, GBS) and *Escherichia coli* K1 are the predominant causes of meningitis and are responsible for roughly 40% and 30% of cases, respectively (Ouchenir et al., 2017; Bundy et al., 2023). While vaccination has markedly reduced mortality in childhood meningitis, neonatal infections continue to carry high case-fatality rates, especially in low-income regions, and roughly half of the survivors experience lasting neurological deficits (Edmond et al., 2010; Guarnera et al., 2024). The high susceptibility of neonates likely reflects the immaturity of both the adaptive immune system and multiple CNS barriers, including the blood–brain barrier (BBB), the blood–CSF barrier, and the leptomeninges (Saunders et al., 2012; Yang et al., 2023). Understanding host–pathogen interactions in this developmental window is essential for designing strategies to protect the neonatal brain (Kim, 2003).

The leptomeninges forms the surface barrier enveloping the brain and spinal cord. It contains a dense vascular network and large numbers of immune cells, all bathed in

cerebrospinal fluid (CSF). Within the leptomeninges, endothelial cells possess BBB properties, including expression of Claudin-5 (Cldn5), Occludin, and transporters characteristic of CNS microvessels (Mastorakos et al., 2019). At present, the role of leptomeningeal endothelial cells (ECs) in mediating infection-induced host responses, including alterations in barrier properties, is largely unexplored.

The present study focuses on the role of one innate immune receptor, Toll-like receptor 4 (TLR4), in regulating the leptomeningeal response to bacterial meningitis. TLR4 is a central pattern-recognition receptor that detects lipopolysaccharide (LPS), the major outer membrane component of Gram-negative bacteria such as *E. coli* (Medzhitov, 2001; Kawai and Akira, 2007). Activation of TLR4 initiates MyD88- and TRIF-dependent signaling cascades, leading to the induction of proinflammatory cytokines, chemokines, and adhesion molecules that orchestrate leukocyte recruitment to infected tissues (Vallières and Rivest, 1997; Pålsson-McDermott and O'Neill, 2004; Nagyoszi et al. 2010; Casanova et al., 2011). In the context of bacterial meningitis, TLR4 has been shown to mediate both host-protective and pathological responses, including vascular inflammation and leukocyte infiltration (Van Well et al., 2013; Doran et al., 2016; Too et al., 2019; Wang et al., 2023). While these studies established TLR4 as a key driver of meningitis-associated inflammation, the specific contribution of endothelial-intrinsic TLR4 signaling to the host response has not been addressed.

Cldn5 is a prominant tight-junction protein in brain ECs. Originally identified as an endothelial-specific component of the tight junction (Morita et al., 1999), Cldn5 was later shown to be indispensable for restricting paracellular permeability *in vivo*, as *Cldn5*-deficient mice exhibit size-selective leakage of small molecules across the BBB (Nitta et al., 2003). Under physiological conditions, Cldn5 is localized to endothelial cell–cell contacts, but its distribution and stability are dynamically regulated by endocytosis, recycling, and degradation pathways that respond to inflammatory stimuli (Engelhardt and Sorokin, 2009; Coisne and Engelhardt, 2011; Hashimoto et al., 2023). During CNS inflammation and infection, pro-inflammatory cytokines and innate immune receptor activation disrupt tight-junction continuity, presumably to increase tissue access to immune cells. This junctional remodeling includes Cldn5 internalization, but the upstream signaling pathways controlling Cldn5 trafficking remain incompletely understood.

A recent single-cell transcriptome study defined the genomic response of the leptomeninges in a mouse model of neonatal *E. coli* meningitis (Wang et al., 2023). Leptomeningeal ECs exhibited a clear inflammatory transcriptional signature, implicating the leptomeningeal vasculature as both a target and an amplifier of innate immune signals during *E. coli* infection. Whether these innate immune signals originated in ECs and whether these signals directly control tight junction remodeling and vascular leak was not tested.

Here, we study a mouse neonatal meningitis model and cultured CNS ECs (bEnd.3 cells) to test whether endothelial-intrinsic TLR4 signaling (i) orchestrates the multi-cellular response of the leptomeninges to infection and (ii) regulates Cldn5 trafficking and vascular barrier function. In the present work, we (i) profiled cell-type–specific responses in the leptomeninges from WT, endothelial *Tlr4* conditional knockout mice (*Tlr4*^{ECKO}), and macrophage *Tlr4* conditional knockouts (*Tlr4*^{MKO}) using single nucleus (sn)RNA-seq; (ii) performed whole-mount immunostaining to quantify ICAM-1 induction, extravascular tracer leakage, and macrophage activation *in vivo*; (iii) tracked Cldn5 redistribution and NF-κB nuclear translocation in bEnd.3 cells exposed to *E. coli*; (iv) generated CRISPR *Tlr4*^{KO} bEnd.3 lines to assess the TLR4 dependence of NF-κB activation, tight-junction dynamics, and barrier permeability; (v) quantified Cldn5 colocalization with junctional, plasma-membrane, and endosomal/lysosomal markers; (vi) defined TLR4-dependent transcriptional programs in bEnd.3 cells. The results of these experiments establish a framework for understanding the pathophysiology of neonatal meningitis that establishes endothelial TLR4 signaling as a central regulator of both the multi-cellular leptomeningeal response to infection and Cldn5 trafficking and junctional integrity.

Results

Cell-type-specific transcriptional responses of leptomeninges from WT, *Tlr4*^{ECKO}, and *Tlr4*^{MKO} mice to neonatal *E. coli* infection

Moving from brain to skull, the meninges consist of four distinct layers: (1) the pia, a thin, semi-permeable layer that mediates solute exchange between the CNS and cerebrospinal fluid (CSF); (2) the subarachnoid space, a highly vascularized region that contains a high density of immune cells; (3) the arachnoid and its epithelial layer, which form a barrier demarcating the boundary between CNS and non-CNS territories; and (4) the dura, a fibrous layer outside of the CNS with a high density of veins, lymphatics, and immune cells (Figure 1A). The second and third layers constitute the leptomeninges. Upon dissection, the bone and dura readily separate

from the leptomeninges. Taking advantage of this natural cleavage plane, we have optimized whole-mount immunostaining and confocal imaging of the leptomeninges together with a thin slice of underlying cortex, a preparation that preserves the anatomical integrity of the leptomeninges and pia (Figure 1B).

In the *E. coli* meningitis model described below, postnatal day (P)5 mice were given a subcutaneous injection of 20 µl of phosphate buffered saline (PBS) with 120,000 colony forming units of *E. coli* RS218 (O18:K1:H7), a clinical isolate from the cerebrospinal fluid of a neonate with bacterial meningitis (Zhu et al., 2020; Wang et al., 2023) or, as a control, 20 µl of phosphate buffered saline (PBS). This *E. coli* strain was additionally transformed with a plasmid encoding a red fluorescent protein (RFP) to facilitate detection of bacteria in infected tissues. Infected and control mice were sacrificed at P6, 24 hours after inoculation. P5 mice were chosen to approximate the developmental stage of the human newborn blood–brain barrier and immune system as described in Wang et al. (2023). This model recapitulates the main temporal sequence of events in human neonates with bacterial meningitis: peripheral entry of bacteria (e.g., via skin abrasions during birth), hematogenous spread of bacteria (bacteremia), and bacterial seeding of the meninges. The simultaneous presence of bacteria in the periphery implies that bacterial products, such as LPS, arise from both local meningeal and distant peripheral sources and, therefore, that the inflammatory responses of meningeal cells reflect responses to bacterial products from both sources.

To assess the cell-specific role of TLR4 signaling in leptomeningeal endothelial cells and macrophages, we studied two conditional knockout lines: endothelial-specific $Tlr4^{ECKO}$ ($Cdh5^{CreER/+};Tlr4^{fl/-}$) and macrophage-specific $Tlr4^{MKO}$ ($Lyz2^{Cre/+};Tlr4^{fl/-}$) (*Lyz2* is also referred to as *LysM*; Clausen et al., 1999; Monvoisin et al., 2006). Cre specificity was confirmed by crossing each driver line to a *Rosa26-lox-stop-lox-tdTomato-2A-nlsGFP* reporter (Wang et al., 2018). Co-staining these reporter mice with known markers for endothelial cells (Cldn5) and macrophages (CD206) revealed no off-target Cre activity (Figure 1 – figure supplement 1). This analysis also shows that $Cdh5^{CreER}$ produces nearly 100% complete recombination of the *Rosa26* reporter in ECs, whereas $Lyz2^{Cre}$, the most efficient of the published macrophage-specific Cre lines (Abram et al., 2014), recombines the *Rosa26* reporter in only a subset of CD206+ cells (Figure 1 – figure supplement 1).

To profile the transcriptional landscape of the leptomeninges in WT, *Tlr4*^{ECKO}, and *Tlr4*^{MKO} mice with and without meningitis, we performed single-nucleus RNA sequencing (snRNA-seq) on dissected leptomeninges (Supplementary file 1). A UMAP projection of the dataset revealed six major cell classes: three distinct fibroblast populations (Fb-arachnoid1, Fb-arachnoid2, and Fb-pia), arachnoid barrier cells, vascular cells, and immune cells (Figure 1C; Figure 1 – figure supplement 2A–C). Comparison of infected and uninfected conditions showed that *Tlr4*^{ECKO} mice exhibited a global attenuation of infection-induced transcriptional responses across all major leptomeningeal cell types, as judged by the positions of cell clusters in the UMAP (Figure 1D).

At the individual gene level, arachnoid barrier and fibroblast cells displayed highly concordant infection responses (Figure 1E). In WT and *Tlr4*^{MKO} mice, infection induced robust upregulation of inflammatory gene programs in arachnoid barrier and fibroblast cells, whereas *Tlr4*^{ECKO} mice were largely devoid of these responses (Figure 1E). Endothelial cells (ECs) and macrophages followed a similar pattern (Figure 1F and G). Examination of infection-induced NF-κB, TNF-alpha, JAK-STAT, and IFN-gamma signaling gene sets revealed that both ECs and macrophages from *Tlr4*^{ECKO} mice had markedly reduced expression of canonical inflammatory targets (Figure 1H; Figure 1 – figure supplement 2D; Figure 1 – figure supplement 3). Curiously, leptomeningeal cells in uninfected *Tlr4*^{MKO} mice exhibit a transcriptional state that mimics, albeit at a low level, the infection response (Figure 1D-H; Figure 1 – figure supplement 2D). We speculate that this *Tlr4*^{MKO} phenotype could represent an alteration in the baseline level of innate immune signaling in uninfected mice. Together, these findings define a meningitis-associated transcriptional program controlled by endothelial TLR4 signaling that drives inflammatory responses in all of the major leptomeningeal cell types (Figure 1I–J).

Endothelial TLR4 drives ICAM-1 induction, increased vascular permeability, and macrophage activation during neonatal *E. coli* infection

To examine the role of endothelial TLR4 in meningitis-associated responses within the leptomeninges, we used whole-mount imaging to assess markers of vascular permeability and immune activation. Intercellular adhesion molecule-1 (ICAM1) serves as a well-established marker of endothelial activation during infection and inflammation (Bui et al., 2020; Singh et al., 2023). Whole-mount leptomeninges from P6 uninfected and *E. coli* infected WT, *Tlr4*^{ECKO} and *Tlr4*^{MKO} mice revealed robust upregulation of ICAM1 in WT and *Tlr4*^{MKO} mice, whereas *Tlr4*^{ECKO} mice showed little change in ICAM1 levels (Figure 2A–B). These protein-level changes

mirrored the genotype-specific transcriptional differences detected by snRNA-seq (Figure 2 – figure supplement 1A). TLR4-dependent ICAM1 upregulation was also observed in the underlying cortical capillaries (Figure 2 – figure supplement 1B–C). For these and all other immunostaining experiments with mice or with cultured cells, the numbers of mice and the numbers of images used in the analyses are listed in Supplementary file 2.

To assess blood–brain barrier (BBB) integrity within the leptomeninges, we performed systemic injections of sulfo-NHS-biotin, a low molecular weight intravascular tracer. In this assay, perivascular streptavidin staining serves as a readout of vascular leakage (Wang et al., 2019). WT and *Tlr4*^{MKO} mice exhibited marked increases in sulfo-NHS-biotin extravasation upon *E. coli* infection, whereas *Tlr4*^{ECKO} mice showed no change from the uninfected state (Figure 2A–C).

In addition to these endothelial responses, we examined macrophage activation within the leptomeninges and underlying cortex. The ASC protein (Apoptosis-associated speck-like protein containing a CARD; ASC/PYCARD) localizes to leptomeningeal macrophages and brain microglia (Figure 2D). Quantification of the area occupied by ASC+ cells revealed significant increases in infected WT mice within both the subarachnoid space and cortex (Figure 2D and E; Figure 2 – figure supplement 1D–E), whereas infected *Tlr4*^{ECKO} mice exhibited a greatly attenuated response. These findings imply that endothelial TLR4 signaling promotes macrophage activation and associated morphologic changes during *E. coli* meningitis. To further characterize macrophage phenotypes, we stained for CD206, a marker of leptomeningeal macrophages (Figure 2D and E; Figure 2 – figure supplement 1F). Within the leptomeninges, and similar to ASC staining, the area occupied by CD206+ macrophages increased in infected WT mice but showed minimal changes in infected *Tlr4*^{ECKO} mice (Figure 2D–E). In the brain, CD206+ cell were too sparse to reliably quantify (Figure 2 – figure supplement 1F). Together, these results indicate that endothelial TLR4 signaling drives both increased vascular permeability and macrophage activation during neonatal *E. coli* meningitis.

Claudin-5 redistribution in response to *E.coli* in leptomeningeal endothelial cells and in bEnd.3 cells

In our previous description of meningitis-associated responses in the leptomeninges, we observed disorganization and redistribution of Claudin-5 (Cldn5) independent of changes in total Cldn5 levels (Wang et al., 2023). Given the central role of Cldn5 in maintaining BBB integrity,

we investigated whether TLR4-mediated inflammatory signaling contributed to these changes, thereby providing a mechanistic link between inflammation and increased vascular permeability. Consistent with prior findings (Wang et al., 2023), both WT and *Tlr4*^{MKO} mice showed an increase in the area occupied by Cldn5 in the leptomeninges following infection (Figure 3A-B). Strikingly, *Tlr4*^{ECKO} mice showed minimal changes in the distribution of Cldn5, implying that cell-autonomous endothelial TLR4 signaling regulates tight-junction organization. In contrast to Cldn5, Zonula Occludens-1 (ZO-1), an intracellular scaffold that associates with endothelial tight junction (TJ) complexes, remained unchanged during infection (Figure 3 – figure supplement 1), suggesting that Cldn5 reorganization results from selective internalization rather than a generalized disassembly of TJs.

To directly test the link between inflammatory signaling and Cldn5 redistribution, we turned to cultured mouse brain endothelial (bEnd.3) cells, which express both TLR4 and Cldn5 at baseline (Williams et al., 1988; Montesano et al., 1990; Sikorski et al., 1993). Time-course imaging of bEnd.3 cells exposed to live or heat-killed *E. coli* or *Group B Streptococcus* (GBS) revealed a shift of Cldn5 from the plasma membrane to an internal compartment within one hour of bacterial exposure with each of the four conditions (Figure 3C, 3D, and 3E first and third plots). The response to *E. coli* was presumably mediated by TLR4 detection of LPS and the response to *Group B Streptococcus* was presumably mediated by TLR2 detection of lipoteichoic acid. Nuclear translocation of NF-κB was also monitored, and it was greatest with exposure to live *E. coli*, starting within 1 hour and increasing during the 6-hour duration of the experiment, consistent with strong and progressively increasing TLR4 activation (Figure 3C left half, and 3E second plot). Heat-killed *E. coli* produced a more modest nuclear translocation of NF-κB, peaking at 3–6 hours (Figure 3D left half, and 3E fourth plot). Despite the robust internalization of Cldn5 in response to either live or heat-killed GBS, the NF-κB response to GBS was minimal, implying that, in bEnd.3 cells, TLR2-mediated activation of the NF-κB response is weaker than TLR4-mediated activation of the NF-κB response (Figure 3C and D right halves, and 3E second and fourth plots). These results support two key conclusions: (i) Cldn5 redistribution is an early and robust endothelial response to diverse bacteria, detectable within one hour of bacterial exposure, and (ii) this response likely occurs independent of NF-κB nuclear translocation and, therefore, of NF-κB–driven transcriptional changes, suggesting that it could occur as a non-transcriptional mechanism downstream of TLR2 or TLR4 activation.

TLR4 signaling controls NF-κB activation, tight junction dynamics, and barrier integrity in bEnd.3 cells exposed to *E. coli*.

To rigorously test the role of TLR4 signaling in bEnd.3 cells exposed to *E. coli*, we generated a CRISPR knockout of *Tlr4* (Figure 4). To construct this cell line, we first established a bEnd.3 line with constitutive Cas9 expression, followed by lentiviral delivery of single-guide RNAs (sgRNAs) using the sgTrack-mCherry system (see Methods; Hulton et al., 2020). Multiple sgRNAs were designed to target exons 1 and 3 of the mouse *Tlr4* locus, and clonal lines were isolated by fluorescence-activated cell sorting for mCherry expression. Functional loss of TLR4 was assessed by quantifying NF-κB nuclear translocation after bacterial exposure, which was absent in $Tlr4^{KO}$ clones (Figure 4 – figure supplement 1A). Sanger sequencing of cloned PCR products encompassing the site of Cas9 cleavage revealed distinct frameshift (i.e., null) mutations in all *Tlr4* alleles in several clones, and one of these, $Tlr4^{KO}$-m1, was chosen for further study (Figure 4 – figure supplement 1B and C). Immunostaining for Cldn5 and NF-κB in WT and $Tlr4^{KO}$ bEnd.3 cells showed that deletion of TLR4 prevented both NF-κB nuclear translocation and Cldn5 internalization in response to *E. coli* (Figure 4A–D).

To extend the *in vivo* observation indicating that endothelial TLR4 signaling increases vascular permeability in the leptomeninges, we used a cell culture assay to quantify barrier permeability across confluent bEnd.3 monolayers (Dubrovskyi et al., 2013). In this assay, bEnd.3 cells are grown to confluence on biotinylated gelatin and breaks in the monolayer of cells are visualized by adding fluorescent streptavidin to the medium. We note that tight junctions containing Cldn5 are only observed when bEnd.3 cells are grown to confluence Figure 4 – figure supplement 2A). Control experiments showed that the streptavidin signal depended on biotinylated gelatin and on gaps in the cell monolayer (Figure 4 – figure supplement 2B). When bEnd.3 cells were grown to confluence, the monolayer effectively restricted streptavidin access to the underlying biotinylated gelatin substrate (Figure 4 – figure supplement 2B). Application of this assay to WT and $Tlr4^{KO}$ bEnd.3 monolayers that were exposed to *E. coli* showed that loss of TLR4 signaling prevented streptavidin binding to the underlying biotinylated gelatin substrate and preserved tight-junction integrity (Figure 4E and F). Together, these data indicate that TLR4 signaling in cultured brain endothelial cells drives Cldn5 internalization and increases monolayer permeability *in vitro*, mirroring TLR4's role *in vivo*.

Comparisons of Cldn5 localization with junctional, plasma membrane, and trafficking markers in WT and $Tlr4^{KO}$ bEnd.3 cells with or without *E. coli* exposure

Next, we sought to gain a deeper understanding of the cellular localization and specificity of Cldn5 redistribution in bEnd.3 cells by comparing WT and *Tlr4*^{KO} lines. We first examined several other TJ-associated and integral membrane proteins known to be expressed in bEnd.3 cells – ZO-1, β-catenin, glucose transporter 1 (GLUT1), and platelet endothelial cell adhesion molecule-1 (PECAM1) – to assess changes in their colocalization with Cldn5 during *E. coli* exposure (Figure 5A–5C). This analysis was conducted using confocal microscopy with a 40X lens; thus, the designation of "colocalization" is at the resolution of conventional light microscopy. Cellular colocalization was quantified using percent-overlap analysis in ImageJ (see Methods). At baseline, ZO-1 and β-catenin showed an average of ~75% overlap with Cldn5, consistent with their known colocalization at endothelial TJs (Figure 5D, Figure 5 – figure supplement 1A). Strikingly, both of these TJ-associated proteins remained membrane-localized after 4 hours of *E. coli* exposure, while Cldn5 was redistributed to cytoplasmic compartments in WT but not *Tlr4*^{KO} cells (Figure 5A, 5D, Figure 5 – figure supplement 1A).

We next analyzed non-TJ membrane proteins. The glucose transporter GLUT1 showed relatively little overlap with Cldn5 at baseline and was confined to the plate-bound membrane surface (Figure 5B). During *E. coli* exposure, GLUT1 was internalized alongside Cldn5, showing ~75% overlap within cytosolic compartments (Figure 5D, Figure 5 – figure supplement 1A). In contrast, PECAM1, another non-TJ surface marker, retained its plasma-membrane localization during the 4-hour exposure to *E. coli* in both WT and *Tlr4*^{KO} cells (Figure 5C, 5D, Figure 5 – figure supplement 1A). Taken together, these findings reveal distinct specificities of internalization among membrane and membrane-associated proteins dependent on TLR4 signaling in cultured brain endothelial cells.

To identify the intracellular compartments involved in Cldn5 trafficking, we co-stained WT and *Tlr4*^{KO} cells for Early Endosome Antigen 1 (EEA1), Lysosome-associated Membrane Protein 2 (LAMP2), Rab7, and Rab11 to label endosomal and lysosomal vesicles, and for Protein Disulfide Isomerase (PDI) and Receptor-binding Cancer Antigen Expressed on SiSo Cells (RCAS1) to mark the endoplasmic reticulum and Golgi apparatus, respectively (Figure 5E-H) (Stamatovic et al., 2009, 2017; Scott et al., 2014; Shearer and Peterson, 2019; MacDonald et al., 2020). After 4 hours of exposure to *E. coli*, Cldn5 colocalization with LAMP2^{+} vesicles increased dramatically to ~75% overlap, and this colocalization was dependent on TLR4 (Figure 5E and 5F). *E. coli* exposure also produced small increases in Cldn5 colocalization with EEA1 and PDI, to ~20% overlap, which was similarly dependent on TLR4 (Figure 5E-H). *E. coli*

exposure produced little change in the low-level colocalization of Cldn5 with Rab7, Rab11, or RCAS1, and there was little or no effect of TLR4 loss (Figure 5E-H). We interpret the TLR4-dependent increase in Cldn5-EEA1 and Cdn5-LAMP2 overlap as representing the endocytic internalization of Cldn5 and its delivery to lysosomes. We interpret the modest increase in Cldn5-PDI as likely arising from the close proximity of endosomes and lysosomes to the ER, which is present throughout the cytoplasm.

Further insights into the mechanism of Cldn5 endocytosis came from visualizing the internalization of transferrin, cholera toxin subunit B (CTB), and 10-kDa dextran, well-established tracers for clathrin-mediated endocytosis, caveolin-mediated endocytosis, and macropinocytosis, respectively (Figure 5 – figure supplement 1B–C; Johnson and Spence, 2010). Prior to *E. coli* exposure, these tracers and Cldn5 exhibited ~80% overlap at the plasma membrane (Figure 5 – figure supplement 1C). Following *E. coli* exposure, overlap with transferrin and CTB was reduced, implying that Cldn5 internalization is not clathrin- or caveolin-mediated. Overlap with 10-kDa dextran is most consistent with Cldn5 entering cells via a macropinocytosis-like mechanism (Figure 5 – figure supplement 1C). In these experiments, as well as those shown in Figures 3-5, the persistence of the intracellular Cldn5 immunostaining signal suggests that there is little or no degradation of internalized Cldn5. Consistent with this inference, a washout experiment demonstrated that Cldn5 internalization is dynamic and reversible: after internalization of Cldn5 in response to a 1-hour *E. coli* exposure, plasma membrane localization of Cldn5 was restored 3 hours after *E. coli* washout (Figure 5 – figure supplement 1D and E). Together, these results indicate that endothelial TLR4 signaling triggers a highly specific and reversible internalization of Cldn5, providing a potential mechanistic link between inflammatory activation and increased vascular permeability.

Role of TLR4 signaling in the transcriptional response to *E. coli* in bEnd.3 cells

To define the transcriptional programs regulated by endothelial TLR4 in response to *E. coli* exposure, we performed bulk RNA-seq on WT and *Tlr4*^{KO} bEnd.3 cells collected 3 hours after *E. coli* exposure (Figure 6). Principal component analysis revealed separation of datasets based on both bacterial exposure and genotype (WT vs. *Tlr4*^{KO}) (Figure 6 – figure supplement 1A and B). Interestingly, WT and *Tlr4*^{KO} bEnd.3 cells that were not exposed to *E. coli* clustered separately, suggesting that there is likely to be a basal level of TLR signaling even in the absence of *E. coli* exposure. Differential expression analysis in WT bEnd.3 cells showed robust induction of proinflammatory transcripts upon *E. coli* exposure, including *Il6*, *Cxcl2*, *Tnf*, *Icam1*,

and *Ccl2* (Figure 6A), whereas this response was almost completely absent in *Tlr4*^{KO} bEnd.3 cells exposed to *E. coli* (Figure 6B; note the change in axis scales in Figures 6A and 6B). A global comparison of pathway activities between genotypes demonstrated that inflammatory signaling was highly TLR4-dependent: TNFα signaling via NF-κB, IL6–JAK–STAT signaling, and general inflammatory response pathways showed strong activation in WT but not *Tlr4*^{KO} bEnd.3 cells (Figure 6C–F).

We next quantified expression of representative cytokines, chemokines, and adhesion molecules that define endothelial activation. Upon *E. coli* exposure, *Il6*, *Cxcl10*, *Ccl2*, *Cxcl5*, *Cd83*, *Ccl20*, and *Icam1* transcripts were all significantly upregulated in WT bEnd.3 cells following *E. coli* exposure but remained unchanged in *Tlr4*^{KO} bEnd.3 cells (Figure 6G). Heatmap visualization of the Hallmark "TNFα signaling via NF-κB" gene set confirmed that NF-κB–responsive genes, including *Nfkbia*, *Ccl2*, *Il6*, and *Tnfaip3*, were selectively induced in WT cells (Figure 6H). Direct comparisons of fold change between genotypes further demonstrated that induction of nearly all NF-κB target genes was strongly attenuated in *Tlr4*^{KO} cells, confirming the loss of canonical inflammatory signaling (Figure 6I).

To systematically assess the breadth of TLR4-dependent pathways activated by *E. coli* exposure in bEnd.3 cells, we performed single-sample gene set enrichment analysis (ssGSEA) across 50 Hallmark pathways. The pathways most strongly affected by genotype × exposure interactions were IL6–JAK–STAT3 signaling, allograft rejection, inflammatory response, TNFα signaling via NF-κB, and the interferon-gamma response (Figure 6 – figure supplement 1C). Heatmaps of Leading-Edge genes in these pathways further highlighted the broad suppression of cytokine and cell adhesion transcript induction in *Tlr4*^{KO} bEnd.3 cells compared to WT (Figure 6 – figure supplement 1D–F).

Together, these transcriptional analyses identify endothelial TLR4 as the dominant driver of the NF-κB– and IL6–JAK–STAT–dependent gene expression programs that mediate inflammatory activation in response to *E. coli* exposure.

Discussion

This study demonstrates that, in a mouse model of neonatal *E. coli* meningitis, endothelial TLR4 signaling is a key determinant of the inflammatory response in all major

leptomeningeal cell types and of the infection-associated increase in vascular permeability. Using cell-type-specific conditional *Tlr4* knockout models, leptomeningeal single-nucleus RNA sequencing, and *Tlr4* knockout in bEnd.3 cells, we show that TLR4 activation in ECs directs molecular, cellular, and transcriptional reprogramming of the vascular barrier. At the molecular and cellular levels, endothelial TLR4 activation triggers rapid, selective, and reversible Cldn5 internalization, coincident with increased endothelial permeability. At the transcriptional level, endothelial TLR4 controls NFκB and IL6/JAK/STAT inflammatory programs and cytokine gene expression. These findings establish endothelial TLR4 as the central leptomeningeal sensor of gram-negative bacteria, linking innate immune recognition to barrier dysfunction and to the tissue-wide inflammatory response.

The leptomeningeal response to bacterial infection

Our snRNA-seq analyses revealed a dramatic transcriptome response to neonatal *E. coli* infection across all major leptomeningeal cell types that was broadly attenuated with EC-specific deletion of *Tlr4*. In ECs, TLR4 was required for the induction of canonical immune activation markers, including ICAM1 and leukocyte-recruiting chemokines. In contrast, deletion of *Tlr4* with *Lyz2-Cre* had minimal effect in the mouse meningitis model. Taken together, these data point to endothelial innate immune sensing as the gatekeeper of immune escalation in the leptomeninges. It is possible that macrophage TLR4 signaling in the leptomeninges may augment endothelial signaling or become relevant later in the course of the infection.

Integrating the *in vitro* and *in vivo* datasets, we find that, in bEnd.3 cells, TLR4 activation triggers a rapid (≤1 hour) and reversible internalization of Cldn5, and that $Tlr4^{KO}$ in bEnd.3 cells prevents both NF-κB translocation from cytoplasm to nucleus and Cldn5 redistribution. This effect is selective: with TLR4 activation, ZO-1 and β-catenin remain junctional, PECAM1 remains at the plasma membrane, and GLUT1 co-internalizes with Cldn5, implying protein-specific relocalization. Percent-overlap and tracer analyses support endocytic routing of Cldn5, with prominent LAMP2+ (i.e., endosomal/lysosomal) localization, in a pattern that argues against canonical clathrin/caveolin pathways and is most consistent with macropinocytosis-like uptake. Strikingly, washout of *E. coli* restores Cldn5 to cell-cell junctions within three hours. This dynamic trafficking model is broadly aligned with prior work showing cytokine/chemokine-evoked endocytosis of tight-junction proteins (including claudins and occludin) during EC barrier opening, via Rho/ROCK or caveolae-dependent routes (Stamatovic et al., 2006, 2009, 2012). Functionally, Cldn5 internalization is accompanied by increased barrier permeability, as

measured by streptavidin passage across bEnd.3 monolayers or by Sulfo-NHS-biotin leakage *in vivo*. These findings reveal an EC-intrinsic process in which TLR4 activation leads to tight-junction remodeling and increased vascular permeability. In classic BBB tight-junction biology, Cldn5 is considered a gatekeeper of size-selective permeability (Morita et al., 1999). These findings extend that picture by identifying Cldn5 internalization as a disease-induced process that is rapid, selective, and reversible.

Meningitis and vascular permeability

We speculate that increased endothelial permeability in the leptomeninges could represents a double-edged adaptive response, deleterious when sustained and/or excessive, yet potentially protective when transient, facilitating the regulated passage of immune mediators and immune cells that are needed to combat infection. More generally, increases in vascular permeability may represent a general response to CNS stress or injury. For instance, others have observed reduced BBB integrity in brain regions remote from a focal optic-nerve injury, following transient global ischemia, and in LPS-driven systemic inflammation (Banks et al., 2015; Ju et al., 2018; Smith et al., 2018).

Activation of endothelial TLR4 signaling and the resulting increase in vascular permeability has direct clinical implications for neonatal meningitis. This relationship suggests that endothelial TLR4 signaling contributes causally to CNS injury by promoting loss of barrier integrity, thereby permitting inflammatory cytokines and bacterial products to diffuse into the CNS parenchyma. These findings align with clinical observations in infants with bacterial meningitis, where elevated CSF cytokines (e.g., IL-6, TNFα) and albumin level correlate with poor neurologic outcomes (Garges et al., 2006; Xu et al., 2019; Gao and Hu, 2024). By demonstrating the centrality of endothelial-intrinsic TLR4 signaling, our data highlight the endothelium not merely as a passive target but as a primary effector of neuropathology. These observations raise the possibility that selective modulation of endothelial TLR4 or more proximate regulators of Cldn5 trafficking could preserve vascular integrity, offering a potential avenue for neuroprotection in neonatal meningitis.

Limitations of the study

Several limitations of the present study should be noted. While bEnd.3 cells provide a useful endothelial model, they only partially capture the structural and molecular complexity of the blood–brain barrier (Garcia-Gallardo and Campbell, 2025). In particular, the bEnd.3 culture

system lacks pericytes and astrocytes. Additionally, the study of fixed cells and tissues do not permit detailed analyses of molecular and cellular dynamics. Going forward, live cell imaging of CNS ECs in culture (cell lines and/or acutely isolated cells) and *in vivo* two-photon imaging of the leptomeninges would complement the present studies by revealing dynamic responses in real time. Finally, the present study focused on *E. coli* K1, the dominant Gram-negative neonatal pathogen. Future work could assess TLR signaling in response to other bacterial pathogens, such as Group B Streptococcus.

Concluding remarks

In sum, this study establishes that endothelial TLR4 signaling couples innate immune recognition to inflammatory responses in multiple leptomeningeal cell types, inducing endothelial Cldn-5 internalization and increasing vascular permeability. The rapid and reversible nature of the Cldn5 internalization response implies that tight-junction remodeling is a dynamically regulated process. These observations reframe the innate immune response to neonatal meningitis as largely an endothelial-driven process. These results also highlight potential opportunities to preserve vascular barrier properties by reducing endothelial TLR4 signaling, stabilizing Cldn5 in tight junctions, or dampening IL6–JAK–STAT and NF-κB signaling in endothelial cells (Freitas et al., 2018; Gadina et al., 2018; Zaffaroni and Peri, 2018; Hashimoto et al., 2021).

Methods

Mouse Models and *E. coli* Infection

Mice were maintained on a C57BL/6J background. The endothelial-specific *Tlr4* conditional knockout line (referred to as $Tlr4^{ECKO}$) was generated by crossing $Tlr4^{fl/fl}$ (JAX, stock #024872) mice with $Tlr4^{-/-}$*;Cdh5-CreERT2/+* mice, yielding $Tlr4^{fl/-}$*;Cdh5-CreER/+* offspring. The *Cdh5-CreER* line (Monvoisin et al., 2023) was the same line used in Wang et al. (2023). For macrophage-specific knockouts ($Tlr4^{MKO}$), $Tlr4^{fl/fl}$ mice were bred with $Tlr4^{-/-}$*;Lyz2-Cre/+* mice, yielding $Tlr4^{fl/-}$*;Lyz2-CreER/+* offspring. Littermates lacking Cre were used as controls. The *Lyz2-Cre* line (JAX, stock #004781) was described in Clausen et al. (1999). The *Rosa26-LSL-tdT-2A-GFP* reporter line (JAX, stick #030867) was described in Wang et al. (2018). Neonatal mice were genotyped by PCR and used for the meninges model without sex selection. Mice were housed and handled according to the approved Institutional Animal Care and Use

Committee protocol of the Johns Hopkins Medical Institutions (protocol MO22M375). Meninges snRNA-seq experiments and histological studies used postnatal day 6 (P6) mice with age-matched controls.

Neonatal *E. coli* K1 infection model

To model neonatal meningitis, postnatal day 5 (P5) mice were used, approximating the developmental stage of the human newborn blood–brain barrier and immune system as described in Wang et al. (2023). Litters were randomized to receive a subcutaneous inoculation in the dorsal skin of 2.5×10^5 colony-forming units (CFU) of *E. coli* RS218 (O18:K1:H7) with an RFP-expression plasmid (Zhu et al., 2020) in 20 µL PBS or 20 µL PBS alone. Twenty-four hours later (at P6), mice were euthanized for tissue collection. Brains, meninges, and relevant tissues were harvested, fixed, and processed for immunofluorescence and tracer leakage assays.

Antibodies for tissue staining

Leptomeningeal and cortical whole-mounts were immunostained with the following primary antibodies: mouse anti-Claudin-5 (Alexa Fluor™ 488, ThermoFisher #352588), mouse anti-ZO-1 (Alexa Fluor™ 594, ThermoFisher #339194), rabbit anti-ICAM-1 (CD54, eBioKAT-1, ThermoFisher #14-0542-85), rat anti-CD206 (Bio-Rad MCA2235), rabbit anti-ASC/TMS1 (Cell Signaling Technology #67824S), rat anti-PECAM-1 (BD Pharmingen #553370), rabbit anti-GLUT1 (ThermoFisher MA5-31960), rabbit anti-cleaved Caspase 3 (Cell Signaling Technology, #9664). Alexa dye-conjugated secondary antibodies were from ThermoFisher.

Sulfo-NHS-biotin leakage

For analysis of vascular leakage, mice were injected intraperitoneally with Sulfo-NHS-biotin (30 µl of 20 mg/mL Sulfo-NHS-biotin in PBS per mouse; ThermoFisher 21217) ~15 minutes before sacrifice. After IP injection, the tracer rapidly equilibrates into the systemic circulation.

Immunostaining of leptomeninges whole-mounts

For whole-mount imaging of the leptomeninges and adjacent cortex, a preparation was developed to preserve these structures in their native configuration. After euthanasia, brains (with leptomeninges attached) were fixed by immersion in 1% paraformaldehyde in PBS overnight at 4 °C. The forebrain was then dissected and hemisected, and a thin slice of tissue from the surface of the brain was obtained by making a 300 µm vibratome section parallel to the

surface of the cortex. Tissue slices were permeabilized in 1% Triton X-100/PBS before immunostaining, and blocked with 5% goat or donkey serum, depending on the secondary antibody host species. Primary antibodies were applied at 1:400 dilution, followed by fluorophore-conjugated secondary antibodies. Vascular leakage in mice injected with Sulfo-NHS-biotin was visualized by staining with streptavidin–Alexa Fluor 488 (Thermo Fisher, #S11223).

Confocal microscopy and image acquisition

All images were acquired on a Zeiss LSM 780 laser-scanning confocal microscope controlled by Zeiss Zen software using 20x, 40x, or 63×/1.4 NA oil-immersion objectives. Fluorophores were excited with 405 nm, 488 nm, 561 nm, and 633 nm laser lines, and channels were collected sequentially to minimize spectral overlap. Z-stacks were acquired with step sizes optimized for each staining set; thinner stacks were used for cultured cell monolayers and deeper stacks for leptomeningeal whole-mounts. The pinhole was set to 1 Airy unit. Laser power, gain, and offset settings were maintained at constant values within each experimental cohort (e.g. comparisons across genotypes). For leptomeninges imaging, two fields were imaged per hemisphere. Maximum intensity projections or single optical sections were exported from Zen for quantification and figure preparation.

bEnd.3 cell culture and maintenance

The mouse brain endothelial cell line bEnd.3 (ATCC CRL-2299) was cultured according to the supplier's protocol. Cells were maintained in Dulbecco's Modified Eagle Medium (DMEM; high glucose, 4.5 g/L) supplemented with 10% fetal bovine serum (FBS). Cultures were kept at 37 °C in a humidified 5% CO_2 incubator. Cells were passaged at ~80–90% confluence using 0.05% trypsin–EDTA and reseeded at a split ratio of 1:4–1:6.

CRISPR-Cas9 generation of bEnd.3 *Tlr4*^{KO} cell lines

A bEnd.3-Cas9 monoclonal line was first established by transducing bEnd.3 cells with a lentivirus carrying *Streptococcus pyogenes* Cas9 (Addgene #52962) (Sanjana et al., 2014). Transduced cells were serially diluted to generate monoclonal populations, and Cas9 expression was validated by western blot. Using this Cas9-expressing line, *Tlr4* knockouts were generated by transduction with sgRNAs targeting exon 3 of *Tlr4* delivered with the sgTrack-mCherry lentivirus (Addgene #114013) (Hulton et al., 2020). Transduced cells were sorted by flow cytometry for mCherry expression, seeded in 96-well trays at one cell per well, and

individual colonies were expanded. Genomic DNA was analyzed by PCR amplifying across the mutated region in *Tlr4* exon 3, subcloning the PCR products into a plasmid vector, and sequencing of individual plasmids following colony PCR. A cloned bEnd.3 derivative cell line was considered to be a candidate *Tlr4*^{KO} if none of its cloned PCR products showed the WT sequence and all of the cloned PCR products showed frameshift mutations in *Tlr4* exon 3. Functional loss of TLR4 was confirmed by quantifying NF-κB nuclear translocation after *E. coli* exposure compared to parental controls.

bEnd.3 immunofluorescence

For all experiments involving responses to bacterial exposure, bEnd.3 cells were seeded onto glass coverslips at ~80% confluency two days prior to the start of the experiment to allow them to form a confluent monolayer with tight junctions. After exposure (or not) to *E. coli* or GBS, cells were fixed in 1% paraformaldehyde in PBS for 15 min at room temperature, permeabilized in 0.1% Triton X-100/PBS, and blocked with 5% goat or donkey serum depending on the secondary antibody host species. Primary antibodies were applied at 1:400 dilution overnight at 4 °C, followed by fluorophore-conjugated secondary antibodies. Coverslips were mounted in antifade medium and imaged by confocal microscopy.

Antibodies for bEnd.3 cell immunostaining

Cultured bEnd.3 cells were immunostained with the following primary antibodies: mouse anti-Claudin-5 (Alexa Fluor™ 488, Thermo Fisher #352588), mouse anti-ZO-1 (Alexa Fluor™ 594, Thermo Fisher #339194), rabbit anti-NF-κB p65 (Cell Signaling Technology #8242S), rabbit anti-β-catenin (Cell Signaling Technology #8480), rat anti-PECAM-1 (Thermo Fisher #63-0311-82), rabbit anti-GLUT1 (Thermo Fisher MA5-31960), mouse anti-EEA1 (Cell Signaling Technology #48453T), rabbit anti-LAMP2 (Cell Signaling Technology #34141T), rabbit anti-Rab7 (Cell Signaling Technology #9367T), rabbit anti-Rab11 (Cell Signaling Technology #5589T), rabbit anti-PDI (Cell Signaling Technology #3501T), and rabbit anti-RCAS1 (Cell Signaling Technology #12290T). Primary antibodies were diluted 1:400 in PBS with 1% Triton X-100 and applied overnight at 4 °C, followed by fluorophore-conjugated secondary antibodies (Thermo Fisher). Coverslips were mounted and imaged by confocal microscopy.

bEnd.3 streptavidin leak assay

Barrier permeability was assayed using biotin-conjugated gelatin substrates as described by Dubrovskyi et al. (2013). Bovine gelatin (Sigma, G1393) was diluted to 1% in D-PBS,

prewarmed to 37 °C, and dissolved with stirring in a 70 °C water bath. EZ-Link NHS-LC-Biotin (Thermo Fisher, Cat. No. 21336) dissolved in DMSO (5 mg/mL) was added to the gelatin at a final concentration of 0.5 mg/mL and reacted for 1 hour at room temperature with constant stirring. The solution was clarified by centrifugation (10,000 g, 5 minutes), aliquoted, and stored at –20 °C. For coating, biotinylated gelatin was thawed, diluted in 0.1 M bicarbonate buffer (pH 8.3) to 0.25 mg/mL, sterilized by 0.22 µm filtration, and applied to culture substrates (e.g., 50 µl per well of a 96-well plate, 2 ml per 35 mm dish). Adsorption was performed overnight at 4 °C, followed by PBS washing. Unconjugated gelatin was used as a control. Incorporation of biotin into gelatin was validated using the Pierce Biotin Quantitation Kit (Thermo Fisher, Cat. No. 28005) according to the manufacturer's instructions. bEnd.3 monolayers were grown to confluence on coated coverslips, and control experiments included (i) gelatin without cells, (ii) biotinylated gelatin without cells, (iii) low-density cells on gelatin, and (iv) low- or high-density cells on biotinylated gelatin. To quantify the integrity of the bEnd.3 monolayer, streptavidin–FITC tracer (Thermo Fisher, #11-4317-87) at 2 µg/mL in DMEM was added to the cell culture medium for 5 min, followed by extensive PBS washing and fixation in 1% paraformaldehyde. Samples were immunostained for ZO-1, nuclei were visualized with DAPI, and the coverslips were mounted in antifade solution and imaged by confocal microscopy. Quantification of streptavidin signal was measured as area fraction per field of view. Each condition was repeated in three independent biological replicates, with multiple image fields analyzed per replicate. To ensure comparability across conditions, all images were collected using identical confocal acquisition settings, and exposure times and intensity scaling were maintained constant within each experiment.

bEnd.3 and *E. coli* washout experiments

bEnd.3 cells were exposed to *E. coli* K1 (at a 5:1 ratio of *E.coli*:bEnd.3 cells) in serum-containing DMEM for 1 hour at 37 °C, 5% CO_2. For washout, the medium was removed, and cells were washed extensively with pre-warmed PBS, then returned to fresh complete medium for a 3-hour recovery period. Parallel groups were fixed at 1 hour (no washout) or after the 3-hour washout. Cells were fixed in 1% paraformaldehyde, permeabilized, blocked, and immunostained (e.g., for Cldn5 and ZO-1) as described above, then mounted for confocal imaging. Acquisition settings (laser power, gain, offset, and channel order) were held constant across conditions within each experiment. Quantification of Claudin-5 cytoplasm/plasma membrane ratios followed the CellProfiler pipeline (Stirling et al., 2021), and results were analyzed as $\log_{10}$-transformed single-cell values with p-values calculated using the Wilcoxon

rank-sum test. Three independent biological replicates were performed, with multiple fields analyzed per replicate.

bEnd.3 tracer experiments

This procedure was performed as described (Stamatovic et al., 2006, 2017). Briefly, bEnd.3 monolayers on glass coverslips were preloaded with plasma-membrane–binding/uptake tracers prior to bacterial exposure: Cholera Toxin Subunit B, Alexa Fluor™ 647 conjugate (CTB-AF647; Thermo Fisher, C34778), Transferrin from human serum, Alexa Fluor™ 647 conjugate (Tf-AF647; Thermo Fisher, T23366), or Fixable Dextran, 10,000 MW, Alexa Fluor™ 647 (Dextran-AF647; Thermo Fisher, D22914). Tracers were added in ice-cold complete medium for 30 minutes at 4 °C to allow accumulation at the plasma membrane, excess tracer was removed by gentle washes with PBS, and cells were returned to tracer-free complete medium at 37 °C. Cultures were then exposed to *E. coli* K1 (at a 5:1 ratio of *E.coli*:bEnd.3 cells) for the indicated intervals (e.g., 4 hours) or left unexposed as controls. Cells were fixed in 1% paraformaldehyde, permeabilized, blocked, and immunostained (e.g., for Cldn5 and ZO-1) as described above. Colocalization/overlap with Cldn5 was quantified in FIJI using fixed 100×100 µm ROIs and AND-masking of binarized channels (see “Percent overlap quantification”), with all acquisition parameters (laser power, gain, offset, channel order) held constant within each experiment. Three independent biological replicates were performed, with multiple fields analyzed per replicate.

***E. coli* and GBS preparation and infection of bEnd.3 cells**

Escherichia coli K1 (RS218) and its RFP-expressing derivative (ampicillin-resistant) were cultured in LB broth and on LB agar plates with or without ampicillin, depending on the strain. *Streptococcus agalactiae* (GBS, ATCC 13813) was cultured in brain heart infusion (BHI) broth and on BHI agar plates. For infections, a single colony was grown overnight in the appropriate broth, and a 200 µl aliquot of the overnight culture was diluted into fresh medium and grown for 1 hour at 37 °C. Bacterial density was estimated by optical density at 600 nm, and bacteria were added to the cultured bEnd.3 cells (at a 5:1 ratio of bacteria to bEnd.3 cells) for all experiments. Heat-killed bacteria were prepared in parallel by heating suspensions to 95 °C for 30 min, and bacterial killing was confirmed by plating aliquots to check for the absence of growth. For bacterial exposure experiments, bEnd.3 cells were cultured in the absence of antibiotics in serum-containing medium, and bacteria remained in the culture medium for the duration of all experiments except in designated washout assays.

Image Analysis: nuclear-to-cytoplasmic (Nuc/Cyto) intensity ratio

NF-κB and Ki-67 nuclear translocation was quantified using a custom CellProfiler pipeline (Stirling et al., 2021). Nuclei were segmented by DAPI, cytoplasmic regions were defined as the cell body excluding the nucleus, and mean intensities were measured in both compartments. Ratios of nuclear-to-cytoplasmic (Nuc/Cyto) intensity were computed per cell and $\log_{10}$-transformed for analysis. Output spreadsheets from CellProfiler were imported into R (v4.3) and annotated by parsing file names to assign genotype, clone, treatment, and timepoint metadata. Data from replicate experiments were combined, and box plots were generated to show distributions of single-cell values. Statistical comparisons between conditions were performed using the Wilcoxon rank-sum test. For validation, replicate-level plots were generated, outliers were defined by interquartile range (1.5×IQR) and excluded from simplified representative plots, and a subset of clones and timepoints (e.g., 0, 1, and 3 hours) were displayed for final figures.

Image Analysis: cytoplasmic-to-plasma membrane (Cyto/PM) intensity ratio

Claudin-5 redistribution between the plasma membrane and cytoplasm was quantified in CellProfiler (Stirling et al., 2021) using a custom pipeline. Plasma membrane regions were segmented using ZO-1 as a boundary, while cytoplasmic regions were defined as the cell body excluding the nucleus and plasma membrane masks. Integrated mean intensities of Claudin-5 were measured in both regions, and cytoplasmic-to-plasma membrane (Cyto/PM) ratios were calculated for each cell and $\log_{10}$-transformed for analysis. Output spreadsheets from CellProfiler were imported into R (v4.3) for downstream analysis. File names were parsed to assign genotype, treatment, timepoint, and replicate metadata, and data from replicate experiments were combined. Box plots were generated to display distributions of single-cell values, with statistical comparisons performed using the Wilcoxon rank-sum test. For representative figures, a single replicate per group was shown, and outliers were removed based on the interquartile range (1.5×IQR).

Image Analysis: percent overlap quantification (ImageJ)

Colocalization between Cldn5 and trafficking/endothelial markers (e.g., EEA1, Rab7, Rab11, LAMP2, ZO-1) or tracers was quantified in FIJI (Schindelin et al., 2012) using a scripted workflow. For each field, maximum-intensity–projected channels were processed as follows: images were Gaussian-blurred ($\sigma = 2$), converted to 8-bit, and binarized using fixed thresholds chosen per channel and experiment. Binary masks were generated with “BlackBackground”

enabled and saved for Cldn5 and the comparison marker. Overlap masks were created with Image Calculator (logical AND) between the Cldn5 mask and the marker mask (and, when needed, between Cldn5 and ZO-1). An ROI set comprising nine 100 × 100 μm squares was loaded via the Region of Interest (ROI) Manager and applied uniformly to all images. For each ROI, we recorded raw mean intensities (non-binary images) and, on the binary masks, measured area and mean intensity. "Signal area" was computed as (ROI area × mask mean)/255 for Cldn5 and for the overlap image, providing an area-weighted signal metric. Percent overlap with Cldn5 was then calculated per ROI as 100 × (overlap signal area ÷ Cldn5 signal area). Identical steps were repeated for each endosomal marker or tracer by substituting the corresponding channel and threshold. Outputs were written to CSV and pooled across images/replicates for plotting; statistical comparisons were performed using Wilcoxon rank-sum tests as described in the Statistics section. All acquisition and analysis parameters (thresholds, ROIs, and export settings) were held constant within a given experiment.

Image Analysis: statistics

All image quantifications were performed on raw data exported directly from FIJI or CellProfiler without manual exclusion of individual cells or ROIs, unless otherwise noted for representative plots. For Cyto/PM and Nuc/Cyto ratios, values were $\log_{10}$-transformed prior to statistical testing. Percent overlap measurements were expressed as the fraction of Cldn5-positive signal area colocalizing with the comparison marker within fixed 100 × 100 μm ROIs. For extravascular tracer (Sulfo-NHS-biotin) and ICAM-1 analyses, fluorescence intensity or area fractions were normalized to the ROI area or expressed as fold change relative to WT uninfected controls. For all datasets, each dot represents a single measurement (one cell *in vitro* or one image field *in vivo*), and biological replicates correspond to independent mice or independent cell culture experiments. Statistical comparisons between two groups were performed using the two-sided Wilcoxon rank-sum test (Mann–Whitney U). Where multiple groups were compared, pairwise Wilcoxon rank-sum tests were performed, and p-values are reported in figure panels. Box plots display the median and interquartile range, with all individual data points overlaid. All statistical analyses were conducted in R (v4.3) using ggplot2 and ggpubr packages, with significance set at $p < 0.05$.

snRNAseq libraries and sequencing

For single-nucleus RNA sequencing, leptomeninges were collected as previously described (Wang et al., 2023). In brief, P6 mice were euthanized 24 hours after infection, brains were

rapidly removed, and the leptomeninges were dissected into ice-cold Hibernate-A medium. The leptomeninges were frozen at -80 °C. Single nucleus (sn)RNA-seq libraries were prepared using the PIPseq T20 3' Single Cell RNA Kit v4.0 PLUS (Fluent BioSiences; Clark et al., 2023). Frozen tissue was suspended in homogenization buffer (0.25 M sucrose, 25 mM KCl, 5 mM $MgCl_2$, 20 mM Tricine-KOH,pH 7.8) supplemented with 1 mM DTT, 0.15 mM spermine, 0.5 mM spermidine, EDTA free protease inhibitor (Roche 11836 170 001), 0.5% IGEPAL-630, and 40 U/mL Protector RNase Inhibitor (Sigma, 03335402001). Samples were homogenized in a 2 mL Dounce homogenizer, using 15 strokes with a loose-fitting pestle followed by 30 strokes with a tight-fitting pestle. The sample was filtered through a 10 µm filter (CellTrix, Sysmex, 04-004-2324), and nuclei were pelleted in Low Retention 1.5 mL microcentrifuge tubes (Thermo Scientific, 3451) for 5 min at 500 x g at 4 °C. Nuclei were washed twice with Nuclei Suspension Buffer (supplied in the Fluent BioSciences kit) supplemented with 1% BSA and 40 U/mL Protector RNase Inhibitor. Nuclei were counted, and ~40,000 nuclei (for the T20 kit) or ~20,000 nuclei (for the T10 kit) were used for library production following the Fluent BioSiences protocol. The resulting snRNA-seq libraries were sequenced on an Illumina NovaSeq X Plus sequencer (Supplementary file 1).

Analysis of snRNAseq data

Reads were aligned with the PIPseeker program (Fluent BioSiences, version 3.3.0) using a STAR index based on the GRCm38 mouse genome with addition of Cre sequences (STAR version 2.7.9a). The CellBender program was used to detect empty droplets and remove background (version 0.3.2; Fleming et al., 2023). The SOLO program was used to remove doublets (scVI-tools 1.2.2-post2) (Bernstein et al., 2020). Manual curation was used to further remove potentially mixed (doublet) nuclei. Clusters representing various brain cells were removed from the final data set. The data were normalized using a regularized negative binomial regression algorithm implemented with the SCTransform function (Hafemeister and Satija, 2019). UMAP dimensional reduction was performed using the R uwot package (https://github.com/jlmelville/uwot) integrated into the Seurat R package (Melville, 2022). Data for the various scatter plots were extracted using the Seurat AverageExpression function, and differential gene expression was analyzed using the Seurat FindMarkers function. The Wilcoxon rank sum test was used to calculate p-values. The p-values were adjusted with a Bonferroni correction using all genes in the dataset. Data exploration, analysis, and plotting were performed using RStudio (RStudio Team, 2020), the tidyverse collection of R packages

(Wickham, 2017), and ggplot2 (Wickham, 2009). Dotplots were generated with the default settings, including default normalization.

GSEA analysis

For Gene Set Enrichment Analysis (GSEA; Subramanian et al., 2005), genes were ranked by the fold expression change between control and mutant datasets. The ranked gene list was used to detect enriched gene sets within the Broad Institute Hallmark Gene Sets using the fgsea R package (https://github.com/ctlab/fgsea; Korotkevich et al., 2019).

RNA-seq on WT and *Tlr4*^{KO} bEnd.3 cells: libraries and sequencing

bEnd.3 mouse brain endothelial cells were cultured in 10-cm tissue culture dishes and grown to confluency under standard conditions (37 °C, 5% CO_2). Total RNA was isolated using the Zymo Research RNA purification kit according to the manufacturer's instructions. Briefly, culture medium was aspirated, cells were rinsed once with ice-cold PBS, and 600 µL of the provided lysis buffer with β-mercaptoethanol was added directly to the dish. The lysate was collected by scraping and transferred to a microcentrifuge tube, briefly mixed, and applied to the Zymo spin column. After binding, the column was washed with the supplied wash buffers, including an on-column DNase I treatment step to remove contaminating genomic DNA, and RNA was eluted in 50 µL of DNase/RNase-free water. RNA concentration and purity were assessed by spectrophotometry (A_{260}/A_{280}), and samples were stored at −80 °C. Library construction was performed with the Illumina mRNA stranded kit following the manufacturer's protocol, and sequencing was performed on an Illumina NovaSeqX with a read length of 300 nucleotides.

RNA-seq on WT and *Tlr4*^{KO} bEnd.3 cells: RNA-seq processing and normalization

Gene-level count matrices from bEnd.3 cells were analyzed in R (v4.5) with Bioconductor (v3.21). The study included two genotypes (WT and *Tlr4*^{KO}) under two conditions (control and exposed to *E. coli* for 3 hours), with biological replication per group (WT: 3 control samples and 4 exposed to *E. coli* samples; *Tlr4*^{KO}: 3 control samples and 4 exposed to *E. coli* samples). Counts were normalized using DESeq2's median-of-ratios size-factor method to control for library size/composition effects. A variance-stabilizing transform (VST) was calculated for quality control and visualization only (e.g., PCA, sample-distance heatmaps). All samples were retained for analysis after QC review.

RNA-seq on WT and *Tlr4^{KO}* bEnd.3 cells: Differential expression

To quantify infection responses within each genotype, DESeq2's negative-binomial generalized linear model was fit separately to WT and in *Tlr4^{KO}* data and then control vs. exposed to *E. coli* data were compared. The reported $\log_2$ fold changes are the control vs. exposed to *E. coli* estimates from these genotype-specific analyses. P-values were adjusted for multiple testing with the Benjamini–Hochberg procedure. False-discovery rates (FDR or q-values) are cited throughout. Gene-level WT vs. *Tlr4^{KO}* effect comparisons were visualized by plotting the two genotype-specific fold changes against one another.

RNA-seq on WT and *Tlr4^{KO}* bEnd.3 cells: Pathway activity scoring and statistics

Pathway analyses used the MSigDB Hallmark collection for mouse, retrieved via msigdbr. Single-sample gene-set enrichment (ssGSEA) was performed with GSVA to obtain an activity score for each pathway in each sample. Scores were computed from $\log_2$-scaled normalized counts ($\log_2$ (normalized counts + 1)), using only genes present in both the RNA-seq data and the gene set. For statistical inference, we modeled pathway scores with a linear model that included genotype, infection status, and their interaction. From this model we reported three quantities per pathway: the *E. coli* exposure effect in WT, the *E. coli* exposure effect in *Tlr4^{KO}*, and the genotype x exposure interaction (difference-in-response between genotypes). P-values were adjusted across pathways with the Benjamini–Hochberg procedure. Adjusted values are reported as q-values (FDR).

RNA-seq on WT and *Tlr4^{KO}* bEnd.3 cells: Visualization

Heatmaps were drawn from VST values after centering each gene by its mean (raw z-scores). Within each Hallmark pathway, genes were ranked by the magnitude of the *E. coli* exposure effect (difference of condition means within each genotype), and the top genes were displayed to show the pattern and directionality across groups. Boxplots summarize ssGSEA scores by group. Per-facet annotations show FDRs for WT and *Tlr4^{KO}* infection effects and the interaction term. Figure 6C plots the pathway-level infection responses in WT (x-axis) versus *Tlr4^{KO}* (y-axis), with point size reflecting within-genotype significance and point color indicating interaction FDR. All figures were exported as vector PDFs.

RNA-seq on WT and *Tlr4^{KO}* bEnd.3 cells: Software

Analyses used DESeq2, limma (for pathway-score modeling), SummarizedExperiment, GSVA, msigdbr, pheatmap, ggplot2, and ggrepel within the R/Bioconductor ecosystem.

Data availability

RNA sequence data were deposited in GEO (accession number GSEXXX).

Acknowledgements.

Supported by the Howard Hughes Medical Institute. The authors thank Timothy Phelps (Department of Art as Applied to Medicine, Johns Hopkins Medical School) for the drawing in Figure 1A, the members of the Johns Hopkins Single Cell and Transcriptomics Core Facility for preparing and sequencing RNAseq libraries from bEnd.3 cells, Yanshu Wang and Ying Wang for advice and for assistance dissecting the leptomeninges, Britta Engelhardt (Theodor Kocher Institute) for advice, and Zhongming Li for helpful comments on the manuscript.

References

Abram CL, Roberge GL, Hu Y, Lowell CA. 2014. Comparative analysis of the efficiency and specificity of myeloid-Cre deleting strains using ROSA-EYFP reporter mice. J Immunol Methods 408:89-100.

Banks WA, Gray AM, Erickson MA, Salameh TS, Damodarasamy M, Sheibani N, Meabon JS, Wing EE, Morofuji Y, Cook DG, Reed MJ. 2015. Lipopolysaccharide-induced blood-brain barrier disruption: roles of cyclooxygenase, oxidative stress, neuroinflammation, and elements of the neurovascular unit. J Neuroinflammation 12:223.

Bernstein NJ, Fong NL, Lam I, Roy MA, Hendrickson DG, Kelley DR. 2020. Solo: Doublet Identification in Single-Cell RNA-Seq via Semi-Supervised Deep Learning.
Cell Syst 11:95-101.e5.

Brouwer MC, Tunkel AR, van de Beek D. 2010. Epidemiology, diagnosis, and antimicrobial treatment of acute bacterial meningitis. Clin Microbiol Rev 23:467-492.

Bui TM, Wiesolek HL, Sumagin R. 2020. ICAM-1: A master regulator of cellular responses in inflammation, injury resolution, and tumorigenesis. J Leukoc Biol 108:787-799.

Bundy LM, Rajnik M, Noor A. 2023. Neonatal Meningitis. In StatPearls. Treasure Island, FL (USA): StatPearls Publishing Company,

Casanova JL, Abel L, Quintana-Murci L. 2011. Human TLRs and IL-1Rs in host defense: natural insights from evolutionary, epidemiological, and clinical genetics.
Annu Rev Immunol 29:447-491.

Clark IC, Fontanez KM, Meltzer RH, Xue Y, Hayford C, May-Zhang A, D'Amato C, Osman A, Zhang JQ, Hettige P, Ishibashi JSA, Delley CL, Weisgerber DW, Replogle JM, Jost M, Phong KT, Kennedy VE, Peretz CAC, Kim EA, Song S, Karlon W, Weissman JS, Smith CC, Gartner ZJ, Abate AR. 2023. Microfluidics-free single-cell genomics with templated emulsification. Nat Biotechnol 41:1557-1566.

Clausen BE, Burkhardt C, Reith W, Renkawitz R, Förster I. 1999. Conditional gene targeting in macrophages and granulocytes using LysMcre mice. Transgenic Res 8:265-277.

Coisne C, Engelhardt B. 2011. Tight junctions in brain barriers during central nervous system inflammation. Antioxid Redox Signal 15:1285-1303.

Doran KS, Fulde M, Gratz N, Kim BJ, Nau R, Prasadarao N, Schubert-Unkmeir A, Tuomanen EI, Valentin-Weigand P. 2016. Host-pathogen interactions in bacterial meningitis. Acta Neuropathol 131:185-209.

Dubrovskyi O, Birukova AA, Birukov KG. 2013. Measurement of local permeability at subcellular level in cell models of agonist- and ventilator-induced lung injury. Lab Invest 93:254-263.

Edmond K, Clark A, Korczak VS, Sanderson C, Griffiths UK, Rudan I. 2010. Global and regional risk of disabling sequelae from bacterial meningitis: a systematic review and meta-analysis. Lancet Infect Dis 10:317-28.

Engelhardt B, Sorokin L. 2009. The blood-brain and the blood-cerebrospinal fluid barriers: function and dysfunction. Semin Immunopathol 31:497-511.

Fleming SJ, Chaffin MD, Arduini A, Akkad AD, Banks E, Marioni JC, Philippakis AA, Ellinor PT, Babadi M. 2023. Unsupervised removal of systematic background noise from droplet-based single-cell experiments using CellBender. Nat Methods 20:1323-1335.

Freitas RHCN, Fraga CAM. 2018. NF-κB-IKKβ Pathway as a Target for Drug Development: Realities, Challenges and Perspectives. Curr Drug Targets 19:1933-1942.

Gadina M, Johnson C, Schwartz D, Bonelli M, Hasni S, Kanno Y, Changelian P, Laurence A, O'Shea JJ. 2018. Translational and clinical advances in JAK-STAT biology: The present and future of jakinibs. J Leukoc Biol 104:499-514.

Gao Y, Hu F. 2024. Predictive role of PAR and LAR in refractory suppurative meningitis in infants. BMC Pediatr 24:462.

Garcia-Gallardo A, Campbell M. 2025. Understanding the Blood-Brain Barrier: From Physiology to Pathology. Adv Exp Med Biol 1477:1-33.

GBD 2016 Neurology Collaborators. 2019. Global, regional, and national burden of neurological disorders, 1990-2016: a systematic analysis for the Global Burden of Disease Study 2016. Lancet Neurol 18:459-480.

Garges HP, Moody MA, Cotten CM, Smith PB, Tiffany KF, Lenfestey R, Li JS, Fowler VG Jr, Benjamin DK Jr. 2006. Neonatal meningitis: what is the correlation among cerebrospinal fluid cultures, blood cultures, and cerebrospinal fluid parameters?
Pediatrics 117:1094-1100.

Guarnera A, Moltoni G, Dellepiane F, Lucignani G, Rossi-Espagnet MC, Campi F, Auriti C, Longo D. 2024. Bacterial Meningoencephalitis in Newborns. Biomedicines 12:2490.

Hafemeister C, Satija R. 2019. Normalization and variance stabilization of single-cell RNA-seq data using regularized negative binomial regression. Genome Biol 20:296.

Hashimoto Y, Campbell M, Tachibana K, Okada Y, Kondoh M. 2021. Claudin-5: A Pharmacological Target to Modify the Permeability of the Blood-Brain Barrier.

Biol Pharm Bull 44:1380-1390.

Hashimoto Y, Greene C, Munnich A, Campbell M. 2023. The CLDN5 gene at the blood-brain barrier in health and disease. Fluids Barriers CNS 20:22.

Hulton CH, Costa EA, Shah NS, Quintanal-Villalonga A, Heller G, de Stanchina E, Rudin CM, Poirier JT. 2020. Direct genome editing of patient-derived xenografts using CRISPR-Cas9 enables rapid in vivo functional genomics. Nat Cancer 1:359-369.

Johnson I, Spence MTZ. 2010. Probes for Endocytosis, receptors, and ion channels. In The Molecular Probes Handbook: A Guide to Fluorescent Probes and Labeling Technologies. (Life Technologies), pp. 739-772.

Ju, F., Ran, Y., Zhu, L., Cheng, X., Gao, H., Xi, X., Yang, Z., and Zhang, S. 2018. Increased BBB Permeability Enhances Activation of Microglia and Exacerbates Loss of Dendritic Spines After Transient Global Cerebral Ischemia. Front Cell Neurosci 12, 236.

Ju F, Ran Y, Zhu L, Cheng X, Gao H, Xi X, Yang Z, Zhang S. 2018. Increased BBB Permeability Enhances Activation of Microglia and Exacerbates Loss of Dendritic Spines After Transient Global Cerebral Ischemia. Front Cell Neurosci 12:236.

Kawai T, Akira S. 2007. TLR signaling. Semin Immunol 19:24-32.

Kim KS. 2003. Pathogenesis of bacterial meningitis: from bacteraemia to neuronal injury. Nat Rev Neurosci 4:376-385.

Korotkevich G, Sukhov V, Sergushichev A. 2019. Fast gene set enrichment analysis. bioRxiv. DOI: https://doi.org/10.1101/060012

MacDonald E, Savage B, Zech T. 2020. Connecting the dots: combined control of endocytic recycling and degradation. Biochem Soc Trans 48:2377-2386.

Mastorakos P, McGavern D. 2019. The anatomy and immunology of vasculature in the central nervous system. Sci Immunol 4:eaav0492.

Medzhitov R. 2001. Toll-like receptors and innate immunity. Nat Rev Immunol 1:135-145.

Melville J. 2022. Uwot: the uniform manifold approximation and projection (UMAP) method for Dimensionality reduction. 0.1.14. R Package. https://cran.r-project.org/web/packages/uwot/index.html

Montesano R, Pepper MS, Möhle-Steinlein U, Risau W, Wagner EF, Orci L. 1990. Increased proteolytic activity is responsible for the aberrant morphogenetic behavior of endothelial cells expressing the middle T oncogene. Cell 62:435-445.

Monvoisin A, Alva JA, Hofmann JJ, Zovein AC, Lane TF, Iruela-Arispe ML. 2006. VE-cadherin-CreERT2 transgenic mouse: a model for inducible recombination in the endothelium. Dev Dyn 235:3413-3422.

Morita K, Sasaki H, Furuse M, Tsukita S. 1999. Endothelial claudin: claudin-5/TMVCF constitutes tight junction strands in endothelial cells. J Cell Biol 147:185-194.

Nagyoszi P, Wilhelm I, Farkas AE, Fazakas C, Dung NT, Haskó J, Krizbai IA. 2010. Expression and regulation of toll-like receptors in cerebral endothelial cells. Neurochem Int 57:556-564.

Nitta T, Hata M, Gotoh S, Seo Y, Sasaki H, Hashimoto N, Furuse M, Tsukita S. 2003. Size-selective loosening of the blood-brain barrier in claudin-5-deficient mice.
J Cell Biol 161:653-660.

Ouchenir L, Renaud C, Khan S, Bitnun A, Boisvert AA, McDonald J, Bowes J, Brophy J, Barton M, Ting J, Roberts A, Hawkes M, Robinson JL. 2017. The Epidemiology, Management, and Outcomes of Bacterial Meningitis in Infants. Pediatrics 140:e20170476.

Pålsson-McDermott EM, O'Neill LA. 2004. Signal transduction by the lipopolysaccharide receptor, Toll-like receptor-4. Immunology 113:153-162.

RStudio Team. 2020. RStudio: Integrated Development Environment for R. RStudio. PBC, Boston, MA. https://rstudio. com

Sanjana NE, Shalem O, Zhang F. 2014. Improved vectors and genome-wide libraries for CRISPR screening. Nat Methods 11:783-784.

Saunders NR, Liddelow SA, Dziegielewska KM. 2012. Barrier mechanisms in the developing brain. Front Pharmacol 3:46.

Schindelin J, Arganda-Carreras I, Frise E, Kaynig V, Longair M, Pietzsch T, Preibisch S, Rueden C, Saalfeld S, Schmid B, Tinevez JY, White DJ, Hartenstein V, Eliceiri K, Tomancak P, Cardona A. 2012. Fiji: an open-source platform for biological-image analysis. Nat Methods 9:676-682.

Scott CC, Vacca F, Gruenberg J. 2014. Endosome maturation, transport and functions. Semin Cell Dev Biol 31:2-10.

Shearer LJ, Petersen NO. 2019. Distribution and Co-localization of endosome markers in cells. Heliyon 5:e02375.

Sikorski EE, Hallmann R, Berg EL, Butcher EC. 1993. The Peyer's patch high endothelial receptor for lymphocytes, the mucosal vascular addressin, is induced on a murine endothelial cell line by tumor necrosis factor-alpha and IL-1. J Immunol 151:5239-5250.

Singh V, Kaur R, Kumari P, Pasricha C, Singh R. 2023. ICAM-1 and VCAM-1: Gatekeepers in various inflammatory and cardiovascular disorders. Clin Chim Acta 548:117487.

Smith NM, Giacci MK, Gough A, Bailey C, McGonigle T, Black AMB, Clarke TO, Bartlett CA, Swaminathan Iyer K, Dunlop SA, Fitzgerald M. 2018. Inflammation and blood-brain barrier breach remote from the primary injury following neurotrauma. J Neuroinflammation 15:201.

Stamatovic SM, Dimitrijevic OB, Keep RF, Andjelkovic AV. 2006. Protein kinase Calpha-RhoA cross-talk in CCL2-induced alterations in brain endothelial permeability.
J Biol Chem 281:8379-8388.

Stamatovic SM, Keep RF, Wang MM, Jankovic I, Andjelkovic AV. 2009. Caveolae-mediated internalization of occludin and claudin-5 during CCL2-induced tight junction remodeling in brain endothelial cells. J Biol Chem 284:19053-19066.

Stamatovic SM, Sladojevic N, Keep RF, Andjelkovic AV. 2012. Relocalization of junctional adhesion molecule A during inflammatory stimulation of brain endothelial cells. Mol Cell Biol 32:3414-3427.

Stamatovic SM, Johnson AM, Sladojevic N, Keep RF, Andjelkovic AV. 2017. Endocytosis of tight junction proteins and the regulation of degradation and recycling.
Ann NY Acad Sci 1397:54-65.

Stirling, D.R., Swain-Bowden, M.J., Lucas, A.M., Carpenter, A.E., Cimini, B.A., and Goodman, A. 2021. CellProfiler 4: improvements in speed, utility and usability. Bmc Bioinformatics 22. ARTN 433,

Subramanian A, Tamayo P, Mootha VK, Mukherjee S, Ebert BL, Gillette MA, Paulovich A, Pomeroy SL, Golub TR, Lander ES, Mesirov JP. 2005. Gene set enrichment analysis: a knowledge-based approach for interpreting genome-wide expression profiles. Proc Natl Acad Sci U S A 102:15545-15550.

Too LK, Yau B, Baxter AG, McGregor IS, Hunt NH. 2019. Double deficiency of toll-like receptors 2 and 4 alters long-term neurological sequelae in mice cured of pneumococcal meningitis. Sci Rep 9:16189.

Vallières L, Rivest S. 1997. Regulation of the genes encoding interleukin-6, its receptor, and gp130 in the rat brain in response to the immune activator lipopolysaccharide and the proinflammatory cytokine interleukin-1beta. J Neurochem 69:1668-1683.

van Well GT, Sanders MS, Ouburg S, Kumar V, van Furth AM, Morré SA. 2013. Single nucleotide polymorphisms in pathogen recognition receptor genes are associated with susceptibility to meningococcal meningitis in a pediatric cohort. PLoS One 8:e64252.

Wang J, Rattner A, Nathans J. 2023. Bacterial meningitis in the early postnatal mouse studied at single-cell resolution. Elife 12:e86130.

Wang Y, Cho C, Williams J, Smallwood PM, Zhang C, Junge HJ, Nathans J. 2018. Interplay of the Norrin and Wnt7a/Wnt7b signaling systems in blood-brain barrier and blood-retina barrier development and maintenance. Proc Natl Acad Sci U S A 115:E11827-E11836.

Wang Y, Sabbagh MF, Gu X, Rattner A, Williams J, Nathans J. 2019. Beta-catenin signaling regulates barrier-specific gene expression in circumventricular organ and ocular vasculatures. Elife 8:e43257.

Wickham H. 2009. Ggplot2: Elegant Graphics for Data Analysis. New York: Springer-Verlag.

Wickham H. 2017. tidyverse: Easily Install and Load the 'Tidyverse'. 1.2.1. R Package. https://CRAN.R-project.org/package=tidyverse

Williams RL, Courtneidge SA, Wagner EF. 1988. Embryonic lethalities and endothelial tumors in chimeric mice expressing polyoma virus middle T oncogene. Cell 52:121-31.

Xu M, Hu L, Huang H, Wang L, Tan J, Zhang Y, Chen C, Zhang X, Huang L. 2019. Etiology and Clinical Features of Full-Term Neonatal Bacterial Meningitis: A Multicenter Retrospective Cohort Study. Front Pediatr 7:31.

Yang R, Wang J, Wang F, Zhang H, Tan C, Chen H, Wang X. 2023. Blood-Brain Barrier Integrity Damage in Bacterial Meningitis: The Underlying Link, Mechanisms, and Therapeutic Targets. Int J Mol Sci 24:2852.

Zaffaroni L, Peri F. 2018. Recent advances on Toll-like receptor 4 modulation: new therapeutic perspectives. Future Med Chem 10:461-476.

Zhu N, Liu W, Prakash A, Zhang C, Kim KS. 2020. Targeting E. coli invasion of the blood-brain barrier for investigating the pathogenesis and therapeutic development of E. coli meningitis. Cell Microbiol 22:e13231.

Figure legends

Figure 1. Cell-type-specific transcriptional responses of leptomeninges from WT, *Tlr4*^{ECKO}, and *Tlr4*^{MKO} mice to neonatal *E. coli* infection.

(A) Schematic of the leptomeninges.

(B) Immunostaining of P6 mouse leptomeninges viewed as a whole-mount (left) or as a transverse section through a series of Z-planes (right). The vertical black bars indicate the extent of the leptomeninges. Scale bars, 20 µm.

(C) UMAP plot of leptomeninges snRNAseq from WT, *Tlr4*^{ECKO}, and *Tlr4*^{MKO} mice at P6, from both uninfected control and with *E. coli* infection, with cell clusters identified (see Figure 1 – figure supplement 1A-C). N=126,235 nuclei. Fb, fibroblast.

(D) UMAP comparison of P6 leptomeninges snRNAseq from control vs. 24-hour *E. coli* infected mice of the indicated genotypes.

(E) snRNAeq from four leptomeninges cell clusters (Fibroblast-arachnoid1, Fibroblast-arachnoid2, Fibroblast-pia, and Arachnoid barrier cells) showing differentially expressed genes in control vs. *E. coli* infected mice of the indicated genotypes at P6.

(F and G) As in panel (E) except for ECs (F) and macrophages (G). DEGs, differentially expressed genes.

(H) As in panel (F) and (G) except DEGs were related to NFkB and TNF-alpha signaling.

(I) Summary of transcriptional responses of leptomeninges from WT, *Tlr4*^{ECKO}, and *Tlr4*^{MKO} mice to *E. coli* infection.

(J) Summary of the effects of TLR4 signaling in leptomeningeal ECs.

Figure 2. Endothelial TLR4 drives ICAM-1 induction, increased vascular permeability, and macrophage activation during neonatal *E. coli* infection.

(A) Whole-mount leptomeninges from P6 WT, *Tlr4*^{ECKO}, and *Tlr4*^{MKO} mice, control or *E. coli* infected, immunostained for Cldn5 and ICAM-1 (upper panels) or immunostained for Cldn5 and incubated with fluorescent streptavidin (lower panels) to visualize the fate of intravascular sulfo-NHS-biotin. Scale bars: 20 µm.

(B) Quantification of ICAM1 immunostaining relative to WT controls, as shown in (A).

(C) Quantification of extravascular streptavidin binding relative to WT controls, as shown in (A).

(D) Whole-mount leptomeninges from P6 WT and *Tlr4*^{ECKO} mice, control or *E. coli* infected, immunostained for Cldn5 and either ASC or CD206 to visualize macrophages. Scale bars: 20 µm.
(E) Quantification of ASC+ area (upper) and CD206+ area (lower), as shown in (D).
Box plots show the median, interquartile range, and all individual data points. Each data point represents one image from a single mouse, with two locations imaged per mouse. Statistical comparisons (p-values) were calculated with the Wilcoxon rank-sum test. ns, non-significant ($p > 0.05$).

Figure 3. Claudin-5 redistribution in response to *E.coli* in leptomeningeal endothelial cells and in bEnd.3 cells.
(A) Whole-mount leptomeninges from P6 WT, *Tlr4*^{ECKO}, and *Tlr4*^{MKO} mice, control or *E. coli* infected, immunostained for Cldn5. Scale bars, 20 µm.
(B) Quantification of Cldn5+ area in the leptomeninges, as shown in (A).
(C) Control bEnd.3 cells and bEnd.3 cells exposed to live *E. coli* or live *group B Streptococcus* (GBS) for 1–6 hours were immunostained for Cldn5 and NF-κB. Scale bars, 20 µm.
(D) Control bEnd.3 cells and bEnd.3 cells exposed to heat-killed *E. coli* or heat-killed *group B Streptococcus* (GBS) for 1–6 hours were immunostained for Cldn5 and NF-κB. Scale bars, 20 µm.
(E) Quantification of experiments shown in (C) and (D). First plot, quantification of $\log_{10}$-transformed cytoplasmic-to-plasma membrane (Cyto/PM) intensity ratio for Cldn5 in bEnd.3 cells exposed to live *E. coli* for the indicated time in hours. Second plot, quantification of $\log_{10}$-transformed nuclear-to-cytoplasmic (Nuc/Cyto) intensity ratio for NF-κB in bEnd.3 cells exposed to live GBS for the indicated time in hours. The third and fourth plots are analogous to the first and second plots, except that bEnd.3 cells were exposed to heat-killed (HK) *E. coli* or GBS.
Box plot in (B) shows median, interquartile range, and all individual data points. Each *in vivo* data point represents one image from a single mouse, with two locations imaged per mouse. For plots in (E), each data point represents a single bEnd.3 cell analyzed from representative images in three biological replicates. Statistical comparisons (p-values) were calculated with the Wilcoxon rank-sum test. ns, non-significant ($p > 0.05$).

Figure 4. TLR4 signaling controls NF-κB activation, tight junction dynamics, and barrier integrity in bEnd.3 cells exposed to *E. coli*.

(A) WT and *Tlr4*^{KO} bEnd.3 cells, either not exposed to *E. coli* (control) or exposed to *E. coli* for 1 hour or 4 hours, were fixed and immunostained for Cldn5 and NF-κB and stained with DAPI. Scale bars: 20 μm.
(B) WT and *Tlr4*^{KO} bEnd.3 cells, either not exposed to *E. coli* (control) or exposed to *E. coli* for 1 hour or 4 hours, were fixed and immunostained for Cldn5 and ZO-1 and stained with CellTrace. Scale bars: 20 μm.
(C) Quantification of $\log_{10}$-transformed nuclear-to-cytoplasmic (Nuc/Cyto) NF-κB intensity ratio in WT and *Tlr4*^{KO} bEnd.3 cells, with or without exposure to *E. coli*, as shown in (A).
(D) Quantification of $\log_{10}$-transformed cytoplasmic-to-plasma membrane (Cyto/PM) Cldn5 intensity ratio in WT and *Tlr4*^{KO} bEnd.3 cells, with or without exposure to *E. coli*, with ZO-1 marking the plasma membrane, as shown in (B).
(E) WT and *Tlr4*^{KO} bEnd.3 cells were grown to confluence on biotinylated gelatin-coated coverslips, were or were not exposed to *E. coli* for 4 hours, were then incubated with fluorescent streptavidin, and were finally fixed and immunostained for ZO-1. Representative images are shown with merged (upper) and streptavidin-only (lower) channels. Scale bars: 20 μm.
(F) Quantification of streptavidin+ area in WT and *Tlr4*^{KO} bEnd.3 cells with or without exposure to *E. coli*, as shown in (E). Wells coated with gelatin alone or biotinylated gelatin (without cultured cells) served as negative and positive controls, respectively.
Box plots show median, interquartile range, and all individual data points. Each data point represents a single cell (C and D) or one image field (F) from representative images in three biological replicates. Statistical comparisons (p-values) were calculated with the Wilcoxon rank-sum test.

Figure 5. Comparisons of Cldn5 localization with junctional, plasma membrane, and trafficking markers in WT and *Tlr4*^{KO} bEnd.3 cells with or without *E. coli* exposure.
(A-C) WT and *Tlr4*^{KO} bEnd.3 cells, either not exposed to *E. coli* (control) or exposed to *E. coli* for 4 h, were fixed and immunostained for Cldn5 and the indicated markers. Scale bars: 20 μm.
(D) Quantification of overlap between Cldn5 and β-catenin, GLUT1, PECAM1, and ZO-1, with each data point representing a 100 μM x 100 μM region of interest (ROI).
(E) WT and *Tlr4*^{KO} bEnd.3 cells, either not exposed to *E. coli* (control) or exposed to *E. coli* for 4 h, were fixed and immunostained for Cldn5 and the indicated markers. Scale bars: 20 μm.
(F) Quantification of overlap between Cldn5 and EEA1, LAMP2, and Rab7, as in (D).
(G) WT and *Tlr4*^{KO} bEnd.3 cells, either not exposed to *E. coli* (control) or exposed to *E. coli* for 4 h, were fixed and immunostained for Cldn5 and the indicated markers. Scale bars: 20 μm.

(H) Quantification of overlap between Cldn5 and Rab11, PDI, and RCAS1, as in (D).
Box plots show median, interquartile range, and all individual data points. Each data point represents one image from representative images in three biological replicates. Statistical comparisons (p-values) were calculated with the Wilcoxon rank-sum test.

Figure 6. In bEnd.3 cells, TLR4 signaling plays a central role in the transcriptional response to *E. coli*.

(A) Volcano plot of differential transcript abundances in WT bEnd.3 cells, with or without exposure to *E. coli*. The plot shows transcript-level $\log_2$ fold change (LFC) on the horizontal axis versus $-\log_{10}$(FDR) on the vertical axis. Red points mark significantly changed transcripts (FDR < 0.05 and |LFC| ≥ 1); grey points are not significant.

(B) Volcano plot of differential transcript abundances in *Tlr4*^{KO} bEnd.3 cells, with or without exposure to *E. coli*, plotted as in (A). Note the change of scale of the vertical and horizontal axes between (A) and (B).

(C) Pathway effect map from ssGSEA Hallmark scores. Each symbol is a pathway. The horizontal axis is the effect of *E. coli* exposure on WT bEnd.3 cells (ΔssGSEA = *E. coli* exposed – not exposed) and the vertical axis is the effect of *E. coli* exposure on *Tlr4*^{KO} bEnd.3 cells. Symbol size encodes the within-genotype significance [max($-\log_{10}$ FDR) across both genotypes], and the color code indicates the genotype × *E. Coli* exposure interaction FDR. The 45-degree diagonal line represents equal effects for the two genotypes.

(D–F) ssGSEA pathway activity based on genotype and *E. coli* exposure for three Hallmark immune response pathways: TNFα signaling via NF-κB (D), Inflammatory response (E), and IL6–JAK–STAT signaling (F). Symbols represent ssGSEA scores for individual samples. The vertical axis shows the interaction FDR score from a linear model for genotype x *E. coli* exposure.

(G) Transcript abundance changes for 12 immune system genes in WT and *Tlr4*^{KO} bEnd.3 cells, with or without exposure to *E. coli.*

(H) Heatmap of transcript abundance changes in WT and *Tlr4*^{KO} bEnd.3 cells, with or without exposure to *E. coli*, for TNFα signaling via the NF-κB pathway. Rows show the transcripts with the greatest changes; values are variance-stabilized transformation (VST) z-scores derived from DESeq2-normalized counts. Columns are arranged by genotype and condition.

(I) Scatterplot showing transcript abundance changes in WT and *Tlr4*^{KO} bEnd.3 cells, with or without exposure to *E. coli*, for TNFα signaling via the NF-κB pathway. Each symbol represents one gene. Red points indicate genes significant for either genotype (FDR < 0.05). The top 15

genes by effect size are labeled. Note the different scales for the horizontal and vertical axes. The diagonal line represents equal effects for the two genotypes.

Supplemental Figure Legends

Figure 1 – figure supplement 1. Specificity of VECad-CreER and Lyz2-Cre in leptomeninges whole-mounts.

(A) *Lyz2Cre*-mediated recombination of the *loxP-stop-loxP* (*LSL*) reporter *ROSA26-LSL-tdT-2A-nlsGFP* shows tdTomato expression in a subset of CD206+ immune cells. (B) *Cdh5Cre*-mediated recombination of the *loxP-stop-loxP* (*LSL*) reporter *ROSA26-LSL-tdT-2A-nlsGFP* shows tdTomato expression in all ECs, visualized with Cldn5 immunostaining. Scale bars, 20 μm.

Figure 1 – figure supplement 2. snRNAseq cell cluster assignments and macrophage transcriptome responses to infection.

(A) UMAP plot of leptomeninges snRNAseq data from WT, *Tlr4*^{ECKO}, and *Tlr4*^{MKO} mice at P6, either uninfected control or with *E. coli* infection, with cell clusters identified. N=126,235 nuclei. Fb, fibroblast.

(B) snRNAseq transcript abundances among the six major leptomeninges cell clusters for a set of 33 genes, for which the transcript abundances distinguish these clusters. We note that cluster Fb-arachnoid2 was originally mis-assigned as a dura fibroblast cluster ("fibroblast dura3") in Wang et al. (2023).

(C) UMAP plots of leptomenenges snRNAseq showing the abundances of transcripts that are highly enriched in each of the six major leptomeninges cell clusters.

(D) snRNAeq for the macrophage cell cluster showing abundant and differentially expressed genes in control vs. *E. coli* infected mice of the indicated genotypes at P6.

Figure 1 – figure supplement 3. Genes regulated by *E. coli* infection in leptomeningeal endothelial cells and macrophages.

(A) Genes regulated by *E. coli* infection in leptomeningeal endothelial cells. Left panel, most differentially regulated genes based on adjusted p-value. Right two panels, most differentially regulated genes based on fold-change.

(B) Genes regulated by *E. coli* infection in leptomeningeal macrophages. Left panel, most differentially regulated genes based on adjusted p-value. Right two panels, most differentially regulated genes based on fold-change.

Figure 2 – figure supplement 1. Infection responses in the leptomeninges and adjacent cerebral cortex in WT and *Tlr4*^{ECKO} mice.

(A) UMAP plot of leptomeninges snRNAseq data from WT and *Tlr4*^{ECKO} mice at P6, either uninfected control or with *E. coli* infection, showing *Icam1* transcripts.

(B) Whole-mount cortical surface, with attached leptomeninges, from P6 WT and *Tlr4*^{ECKO} mice, control or *E. coli* infected, immunostained for Cldn5 and ICAM1. Upper panels, stacked Z-planes at the level of the subarachnoid space; lower panels, stacked Z-planes at the level of the adjacent cerebral cortex. Scale bars, 20 μm.

(C) Quantification of ICAM1 immunostaining in the subarachnoid space and adjacent cerebral cortex, as shown in (B). Note the different scales for the vertical axis in the two plots.

(D) As in (B), except immunostained for Cldn5 and ASC.

(E) Quantification of ASC immunostaining in the cerebral cortex, as shown in the lower row of images in (D).

(F) As in (B), except immunostained for Cldn5 and CD206. These data are not quantified because CD206 cells were so rare in the cortex in all samples that accurate quantification would have been difficult.

Figure 3 – figure supplement 1. ZO1 in leptomeningeal endothelial cells with or without *E. coli* infection.

(A) Whole-mount leptomeninges from P6 WT and *Tlr4*^{ECKO} mice, control or *E. coli* infected, immunostained for Cldn5 and ZO1. Scale bars, 20 μm.

(B) Quantification of ZO1 immunostaining in the subarachnoid space, as shown in (A).

Figure 4 – figure supplement 1. CRISPR KO of *Tlr4* in bEnd.3 cells

(A) Functional testing of three bEnd.3 clones following CRISPR KO of *Tlr4.* For each clone, the TLR4-mediated NFkB response to *E. coli* exposure (migration of NFkB from cytoplasm to nucleus) was quantified by immunostaining, as shown in Figure 3C-E.

(B) Sanger sequencing from two plasmid subclones carrying genomic PCR products encompassing the region targeted by the *Tlr4* guide RNA from bEnd.3-*Tlr4*^{KO}-m1 cells. Each sequencing run shows a distinctive frameshift mutation. The sequences show the WT

sequence on the left and the mutant sequence (with the altered nucleotides in red) on the right. Left, a single nucleotide insertion. Right, a two-nucleotide deletion.
(C) Compendium of ten plasmid subclone sequences from each of the three bEnd.3 clones shown in (A). Each clones shows three distinct alleles, all of which differ from WT and all of which produce a frameshift. No WT sequences were observed in any subclone. These data imply the *Tlr4* gene is present at three copies in bEnd.3 cells, and that each subclone is likely null for *Tlr4* function.

Figure 4 – figure supplement 2. The streptavidin leak assay requires a confluent monolayer of bEnd.3 cells.
(A) Among bEnd.3 cells, junctional localization of Cldn5 requires cell-cell contact as shown by immunostaining of cells grown at different densities.
(B) bEnd.3 cells were grown at either low or high density on biotinylated gelatin-coated coverslips, incubated with fluorescent streptavidin, and then fixed and immunostained for ZO-1. In regions where the bEnd.3 cells had not formed a contiguous network of tight junctions, the streptavidin gained access to the underlying biotinylated gelatin.

Figure 5 – figure supplement 1. Cldn5 dynamics in bEnd.3 cells following exposure to *E. coli*.
(A) The overlap between Cldn5 and β-catenin, GLUT1, PECAM1, and ZO-1, in WT and *Tlr4*^{KO} bEnd.3 cells, either not exposed to *E. coli* (control) or exposed to *E. coli* for 4 hours. Shown here is a more granular quantification of the experiment shown in Figure 5A-D, with each datapoint representing a 100 μM x 100 μM region of interest (ROI).
(B) bEnd.3 cells were pre-incubated for 30 minutes with the indicated fluorescent tracer, then either not exposed to *E. coli* (control) or exposed to *E. coli* for 4 hours, and finally fixed and immunostained for Cldn5. Scale bars, 20 μm.
(C) Quantification of % overlap between tracer and Cldn5 from the experiment shown in (B).
(D) Cldn5 internalization and recovery during 1 hour of *E. coli* exposure, followed by washing away of the *E. coli*, and then an additional 3 hours of incubation in medium without bacteria.
(E) Quantification of the experiment shown in (D). The metric on the y-axis is (cytoplasmic signal – plasma membrane signal)/(cytoplasmic signal + plasma membrane signal). 100% cytoplasmic localization corresponds to 1.0. 100% plasma membrane localization corresponds to -1.0. 50% cytoplasmic localization + 50% plasma membrane localization corresponds to 0.0.

Box plots show median, interquartile range, and all individual data points. Each data point represents one image from representative images in three biological replicates. Statistical comparisons (p-values) were calculated with the Wilcoxon rank-sum test.

Figure 6 – figure supplement 1. Transcriptome analysis of WT and *Tlr4*^{KO} bEnd.3 cells, with or without exposure to *E. coli*.

(A) Principal component analysis showing the relatedness of the 14 bEnd.3 RNAseq samples. Two of the four orange symbols are nearly superimposed.

(B) Pearson correlations for the 14 bEnd.3 RNAseq samples.

(C) Pathway-level effects, showing the difference between WT and *Tlr4*^{KO} bEnd.3 cells for control vs. *E. coli* exposure. Red, false discovery rate (FDR) less than 0.01. Orange, FDR between 0.01 and 0.05. Green, FDR between 0.05 and 0.25. Grey, FDR greater than 0.25.

(D-F) Individual transcript abundances in the 14 bEnd.3 RNAseq samples for three GSEA categories. The transcriptome responses to infection are minimal in *Tlr4*^{KO} bEnd.3 cells.

Supplemental Files

Supplementary file 1. Overview of snRNAseq on leptomeninges.

Supplementary file 2. Numbers of mice and cells used in various experiments.

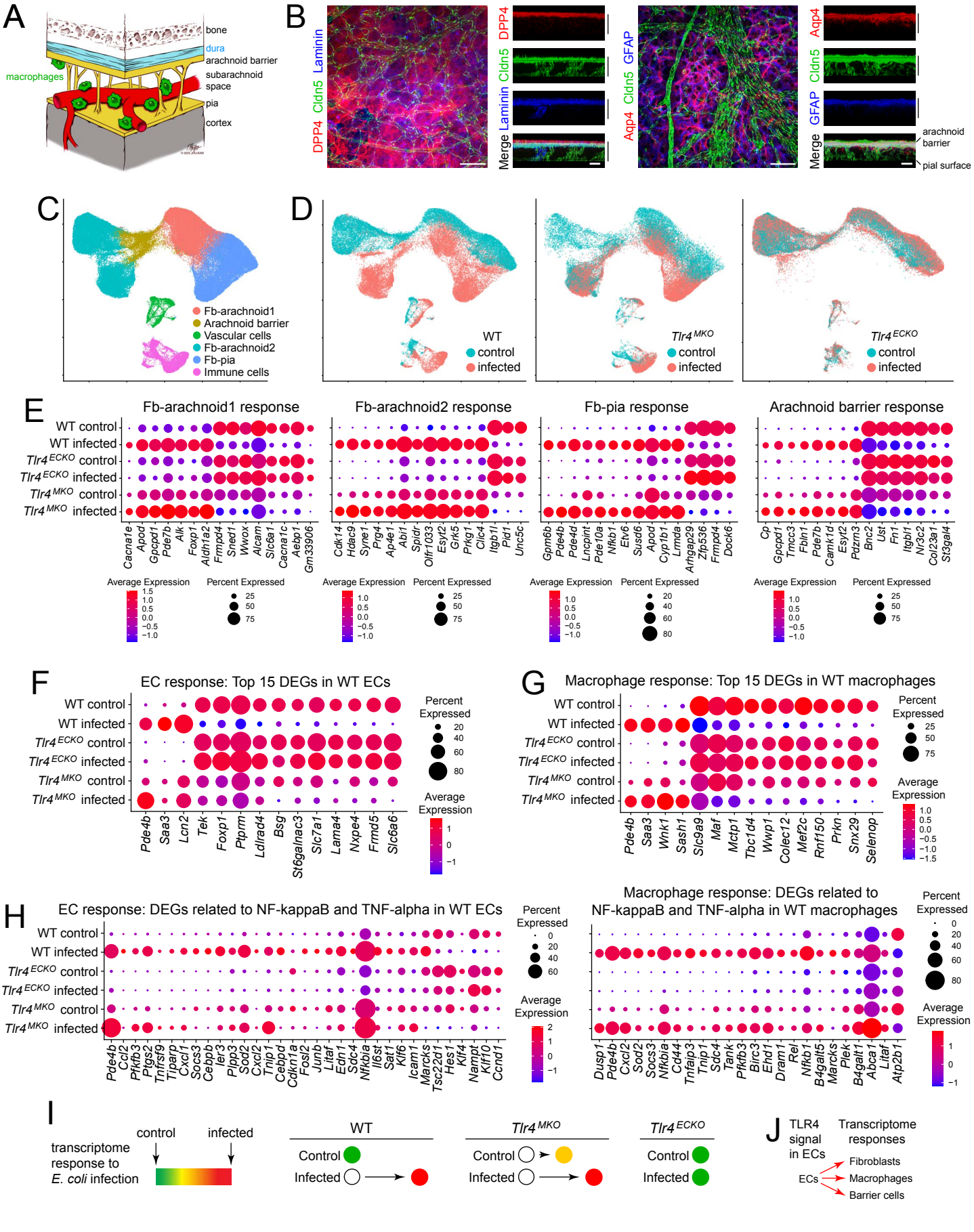

Seegren et al., Figure 1

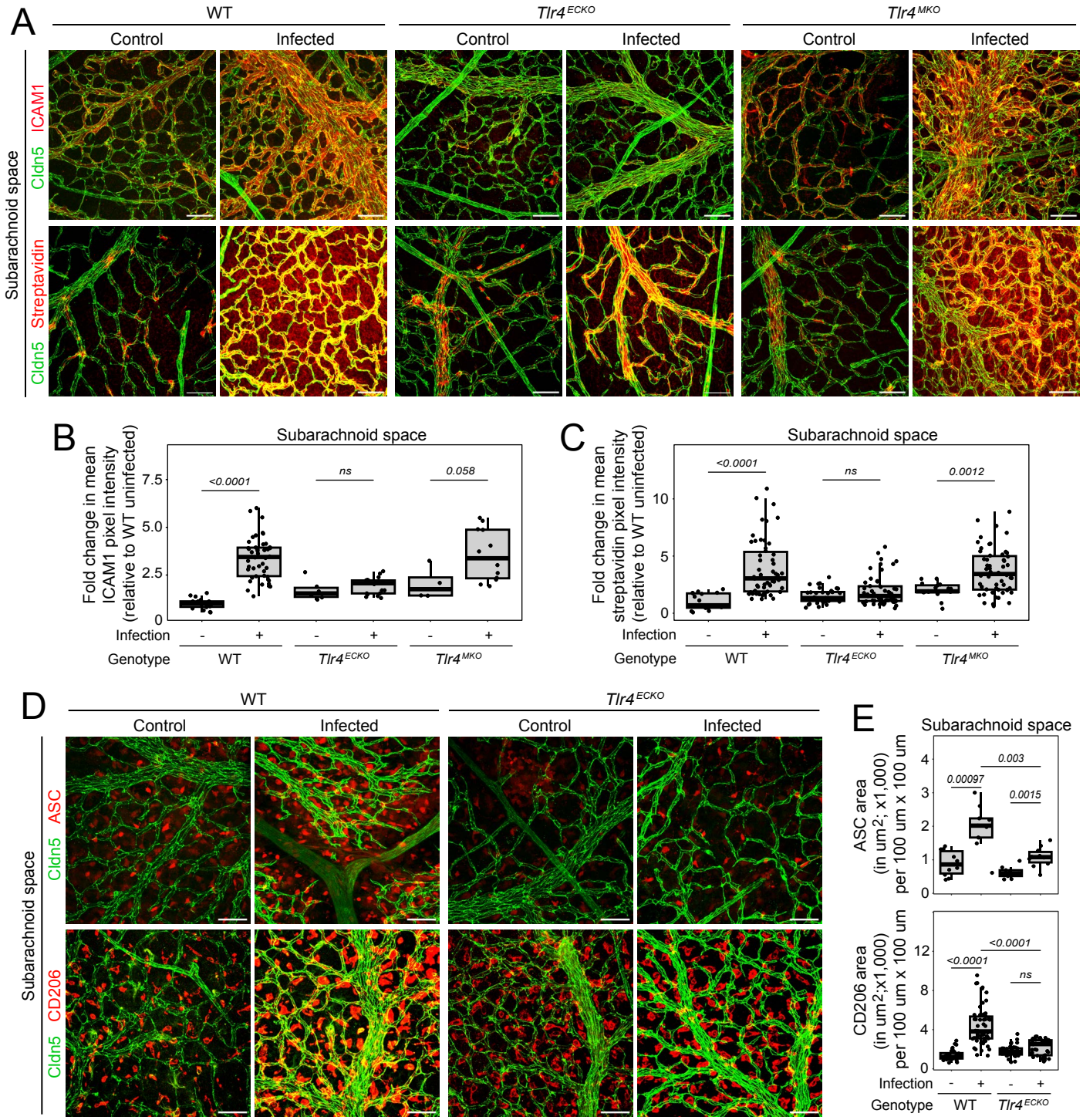

Seegren et al., Figure 2

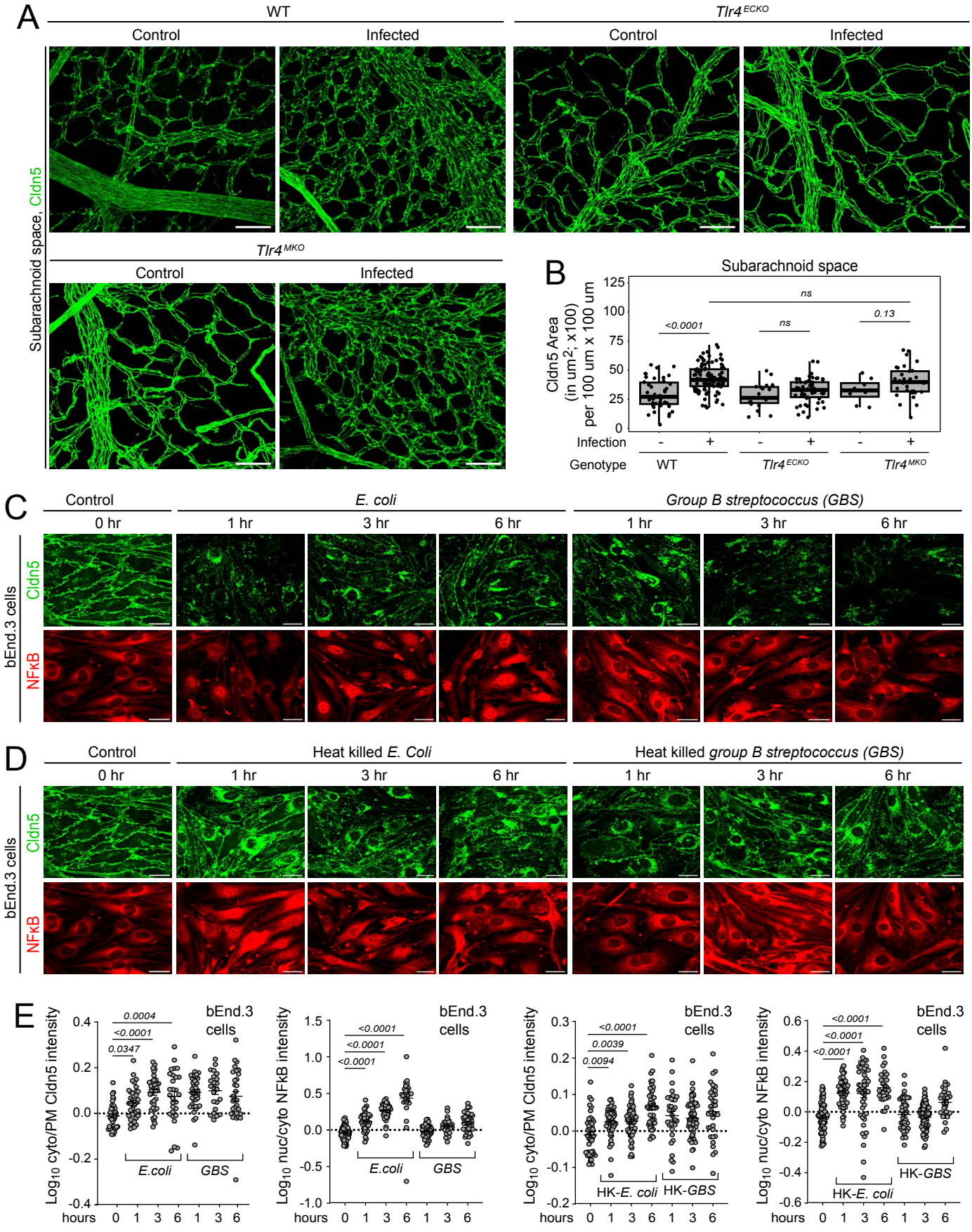

Seegren et al., Figure 3

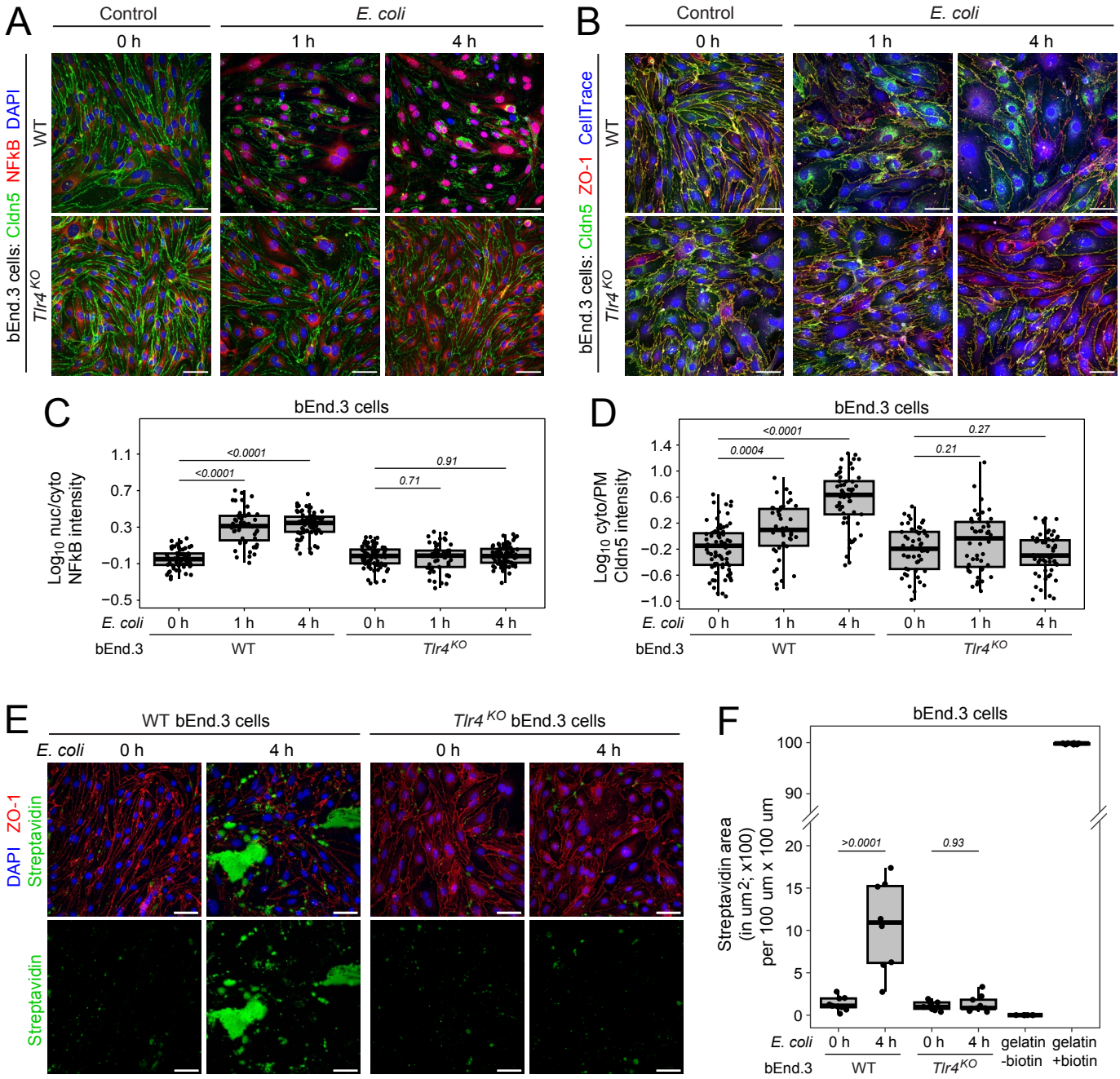

Seegren et al., Figure 4

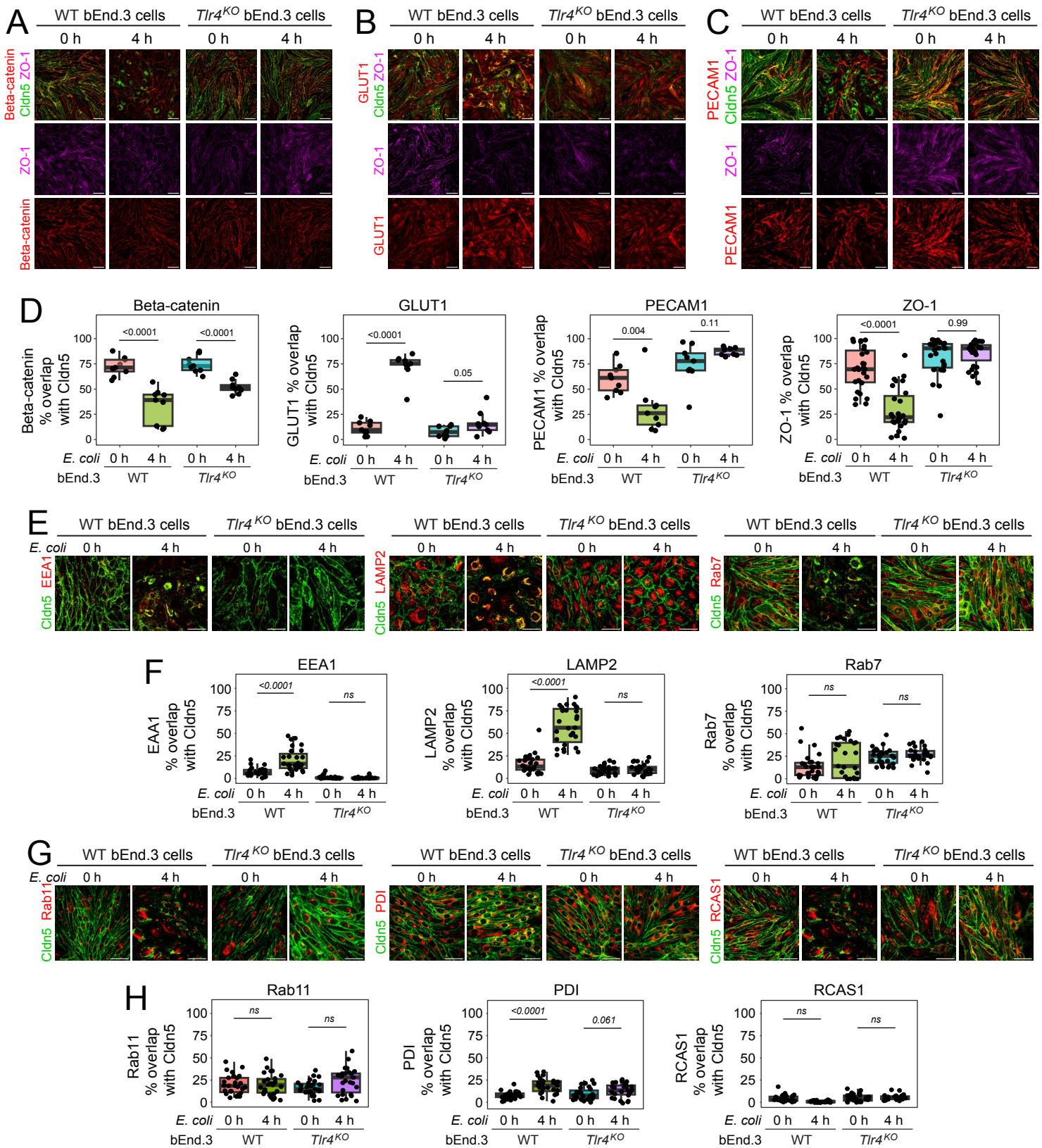

Seegren et al., Figure 5

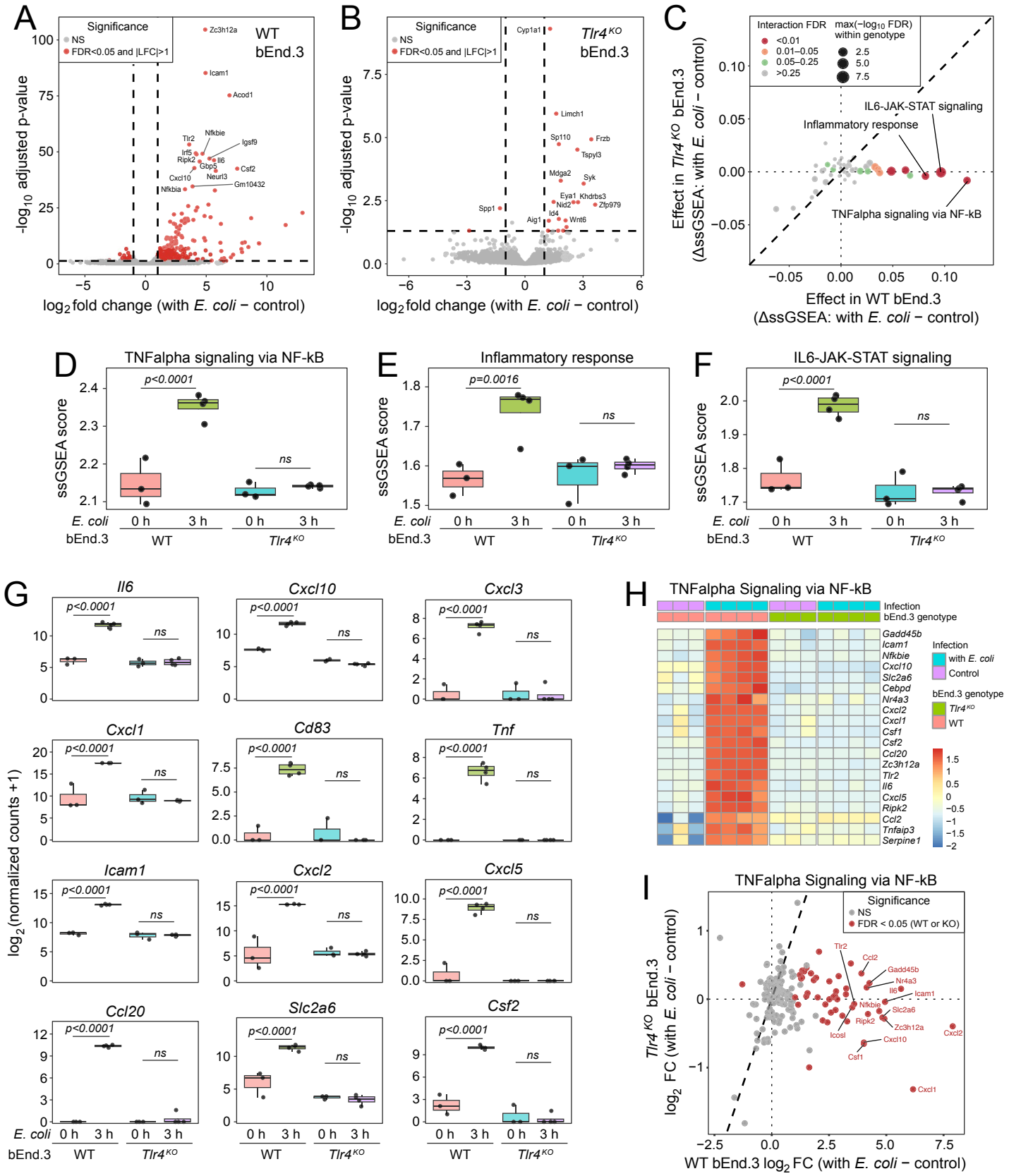

Seegren et al, Figure 6

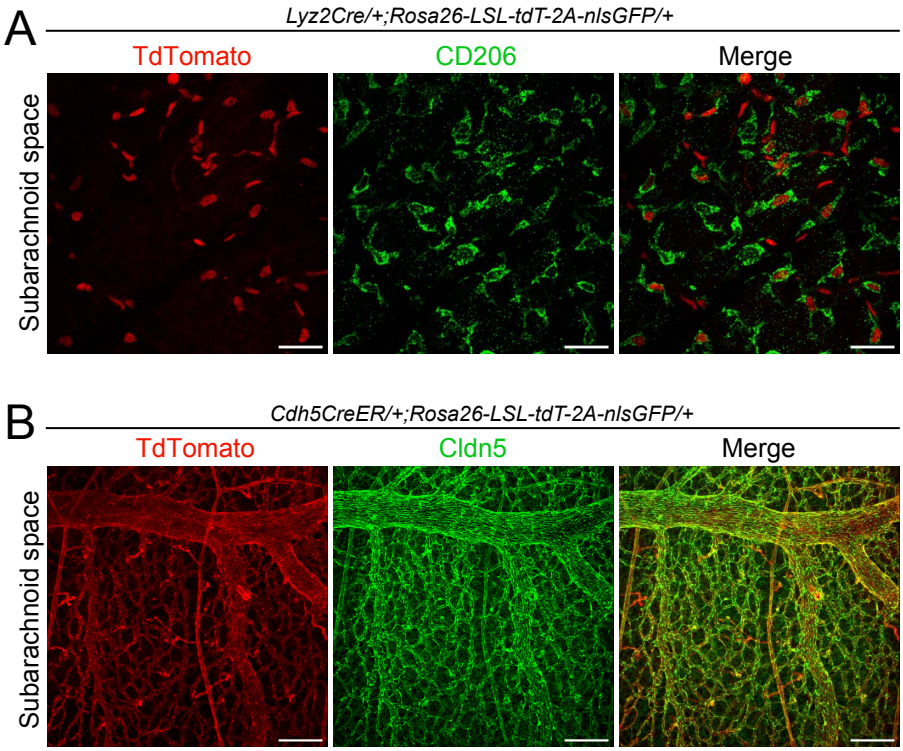

Seegren et al., Figure 1 - figure supplement 1

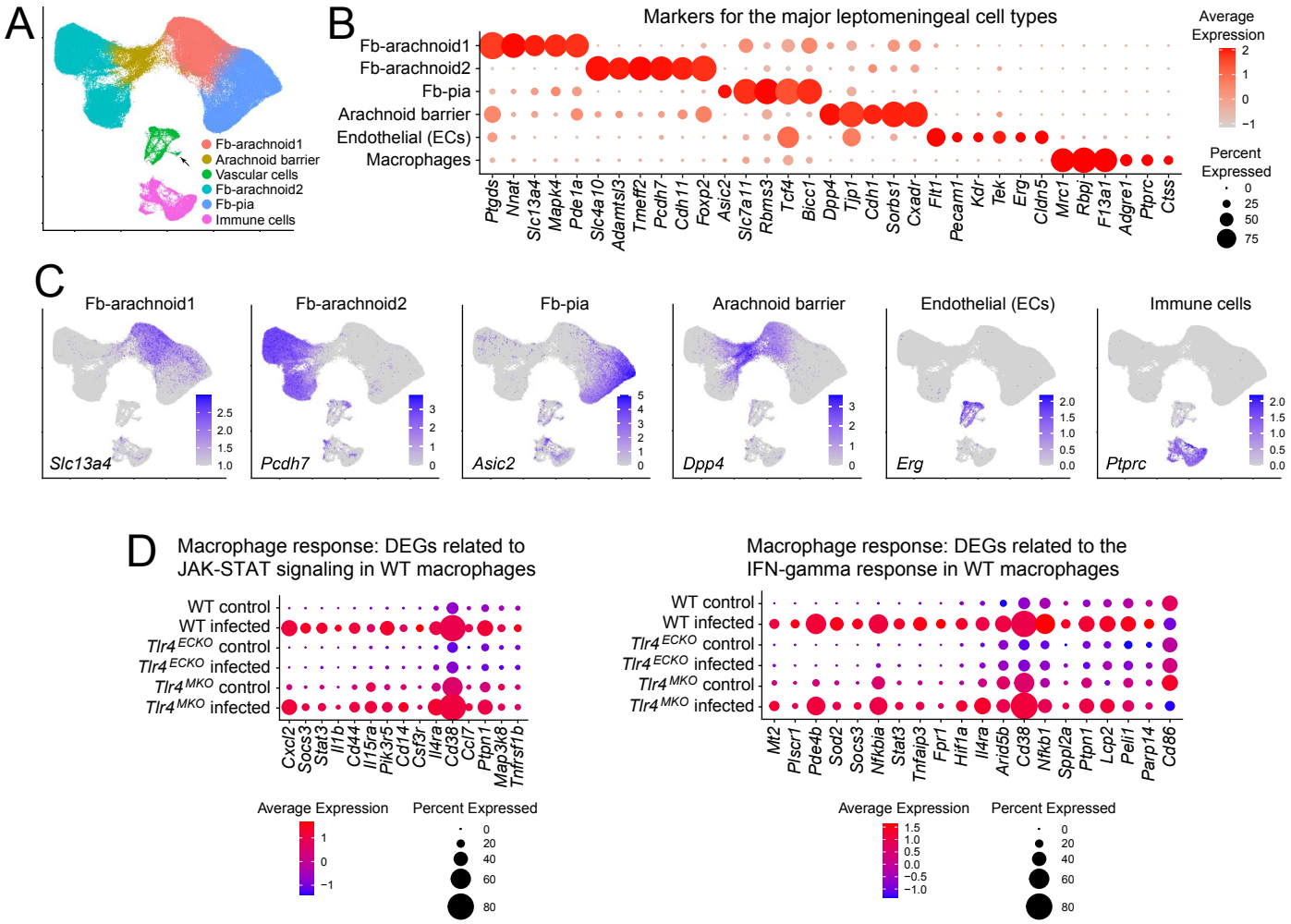

Seegren et al., Figure 1 - figure supplement 2

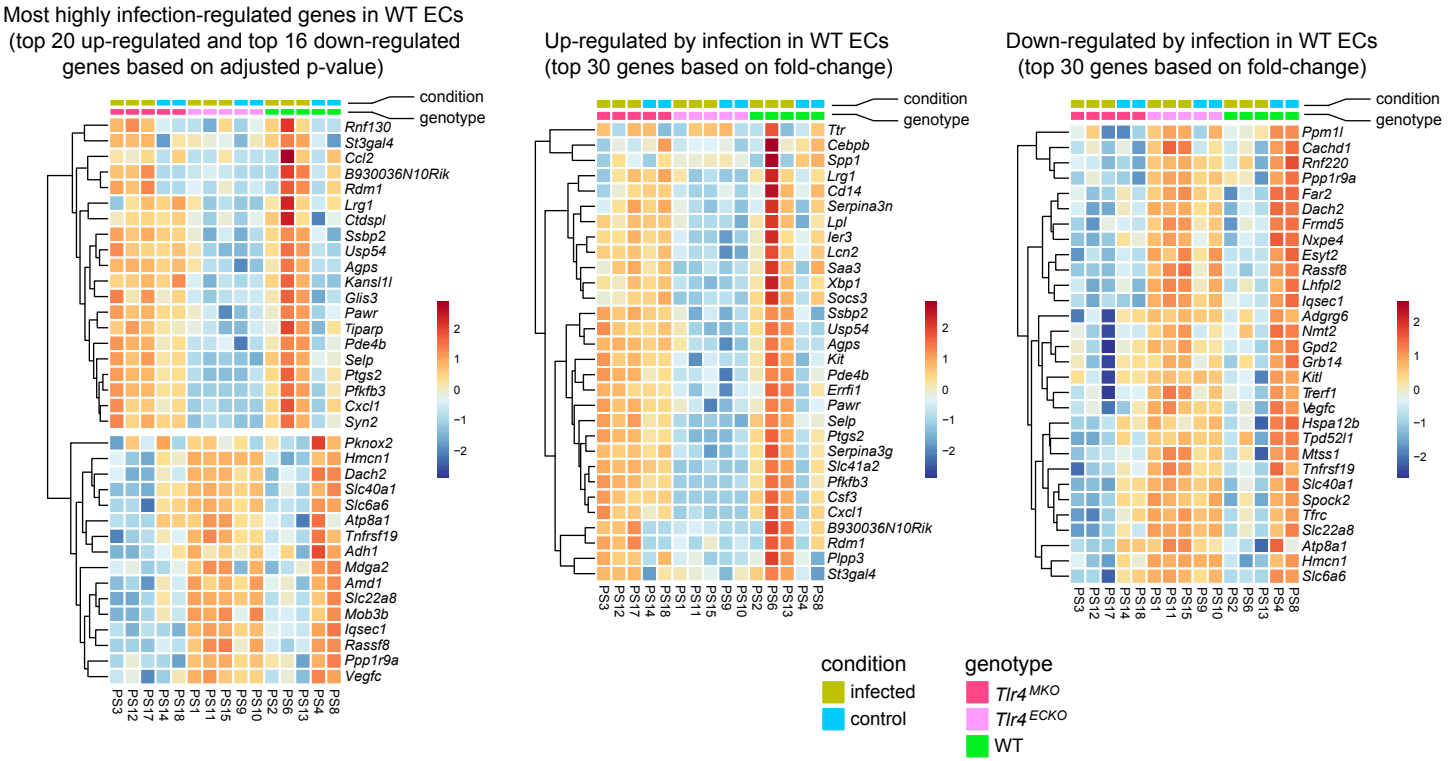

Seegren et al., Figure 1 - figure supplement 3

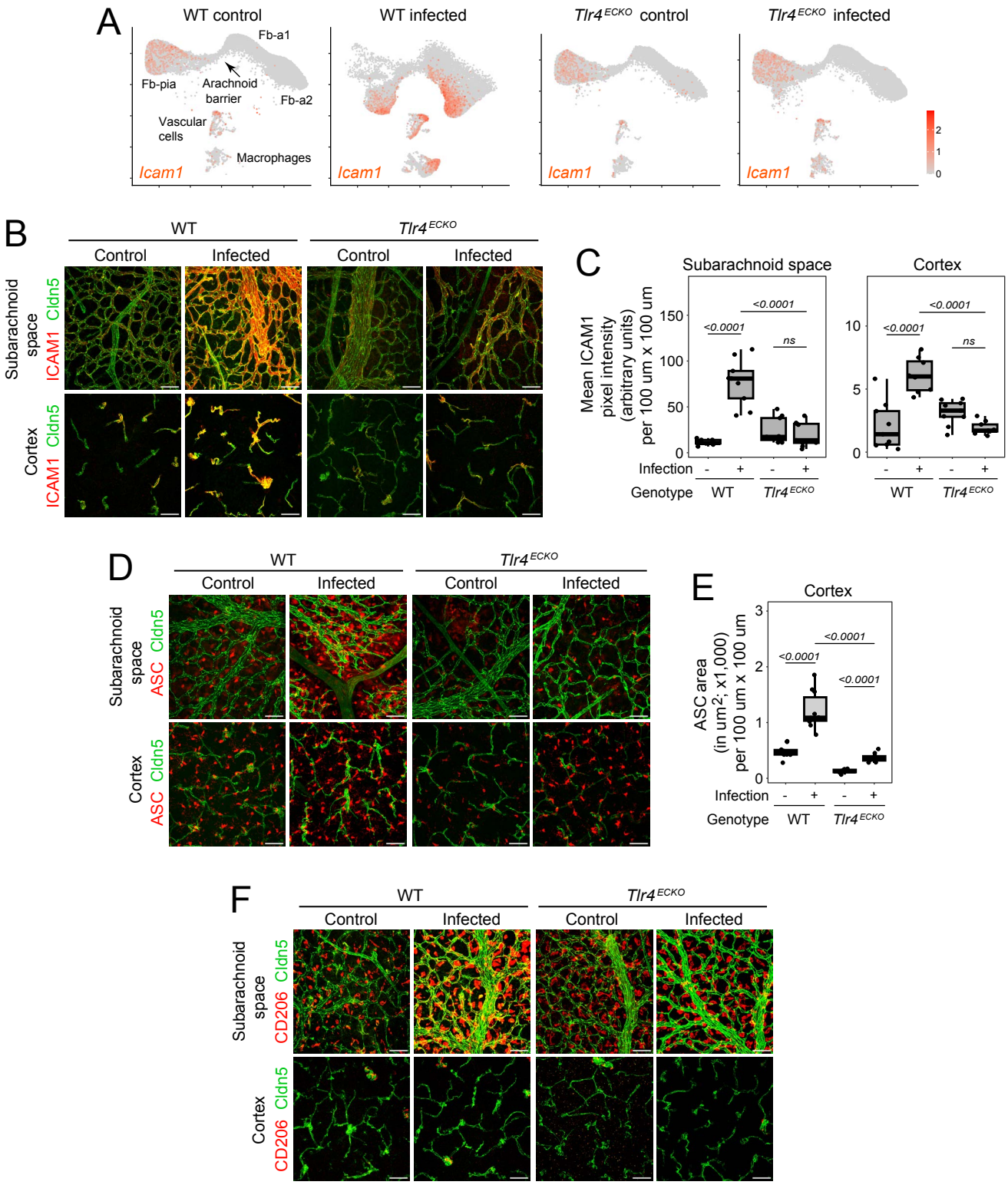

Seegren et al., Figure 2 - figure supplement 1

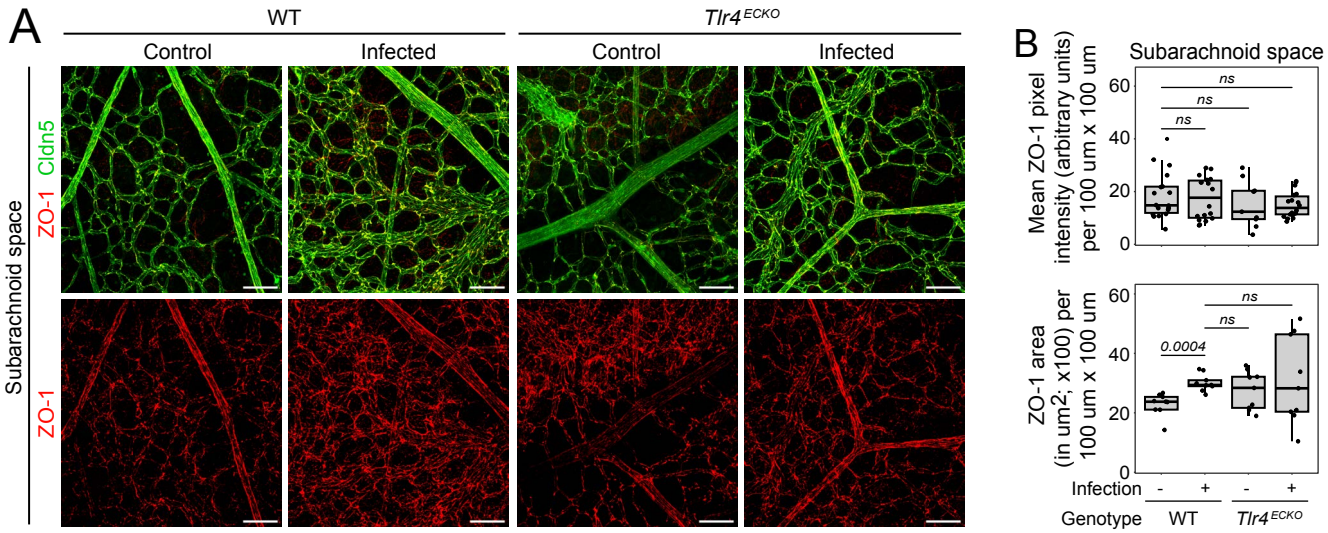

Seegren et al., Figure 3 - figure supplement 1

A

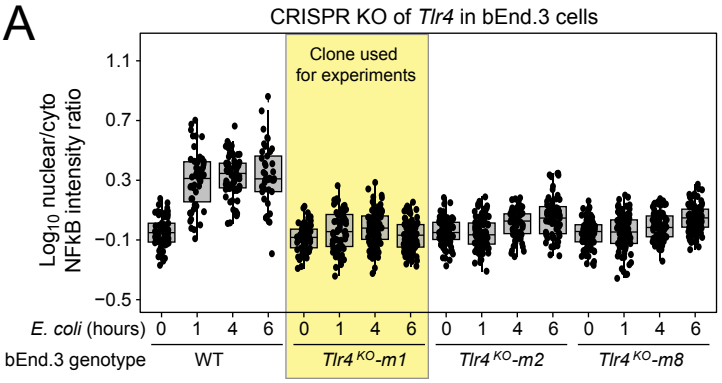

B

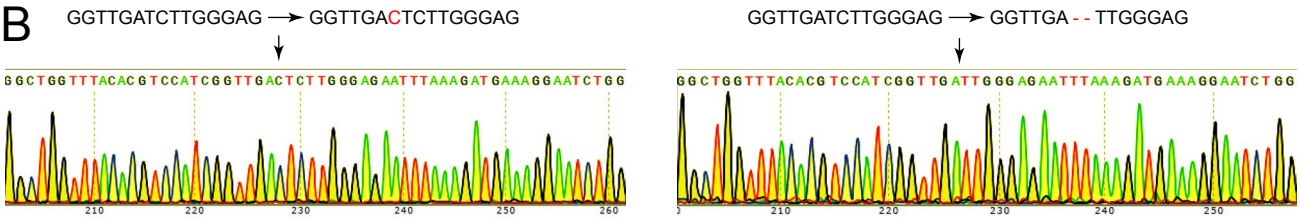

C

Sequence ID	bEnd.3-*Tlr4*^{KO}-m1, Chromosome 4, *Tlr4* Exon 3	Frequency
s1	5'- GGCTGGTTTACACGTCCATCGGTTGACTCTTGGGAGAATTTAAAGATGAAAGGAATCTGG -3'	6/10
s2	5'- GGCTGGTTTACACGTCCATCGGTTGA__TTGGGAGAATTTAAAGATGAAAGGAATCTGG -3'	2/10
s3	5'- GGCTGGTTTACACGTCCATCGGTTGA_C_TGTGAGAATAATTAAAAGATGAGAGGAAGCTGG -3'	2/10
WT	5'- GGCTGGTTTACACGTCCATCGGTTGATCTTGGGAGAATTTAAAGATGAAAGGAATCTGG -3'	0/10
Sequence ID	bEnd.3-*Tlr4*^{KO}-m2, Chromosome 4, *Tlr4* Exon 3	Frequency
s1	5'- GGCTGGTTTACACGTCCATCGGTTGACTCTTGGGAGAATTTAAAGATGAAAGGAATCTGG -3'	3/10
s2	5'- GGCTGGTTTACACGTCCATCGGTTGA__TTGGGAGAATTTAAAGATGAAAGGAATCTGG -3'	5/10
s3	5'- GGCTGGTTTACACGTCCATC____CAATCTTGGGAGAATTTAAAGATGAAAGGAATCTGG -3'	2/10
WT	5'- GGCTGGTTTACACGTCCATCGGTTGATCTTGGGAGAATTTAAAGATGAAAGGAATCTGG -3'	0/10
Sequence ID	bEnd.3-*Tlr4*^{KO}-m8, Chromosome 4, *Tlr4* Exon 3	Frequency
s1	5'- GGCTGGTTTACACGTCCATCGGTTGACTCTTGGGAGAATTTAAAGATGAAAGGAATCTGG -3'	2/10
s2	5'- GGCTGGTTTACACGTCCATCGGTTGA__TTGGGAGAATTTAAAGATGAAAGGAATCTGG -3'	4/10
s3	5'- GGCTGGTTTACACGTCCATC____CAATCTTGGGAGAATTTAAAGATGAAAGGAATCTGG -3'	4/10
WT	5'- GGCTGGTTTACACGTCCATCGGTTGATCTTGGGAGAATTTAAAGATGAAAGGAATCTGG -3'	0/10

Seegren et al., Figure 4 - figure supplement 1

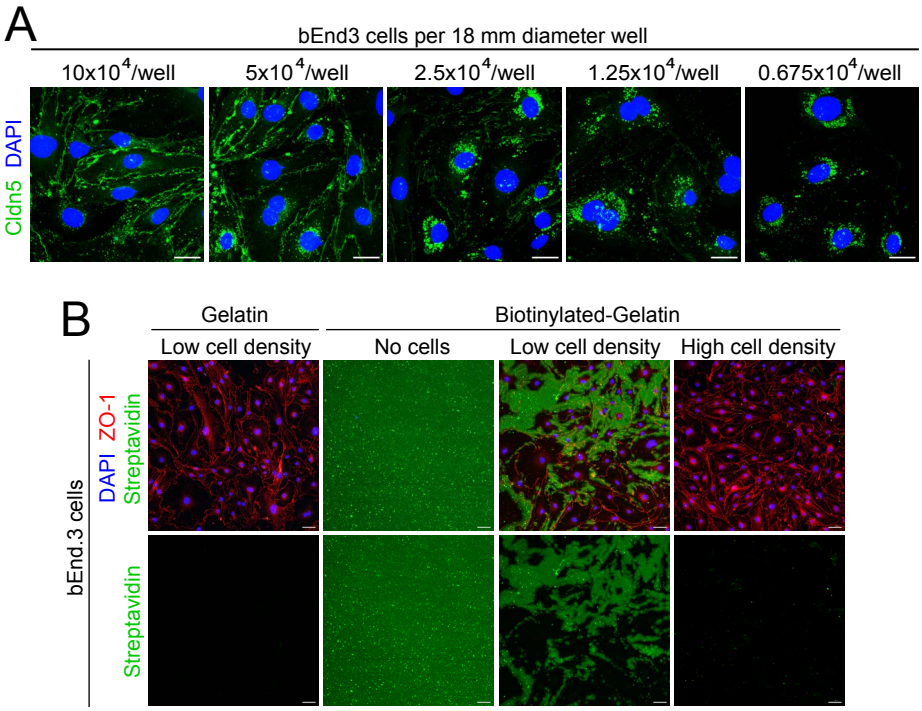

Seegren et al., Figure 4 - figure supplement 2

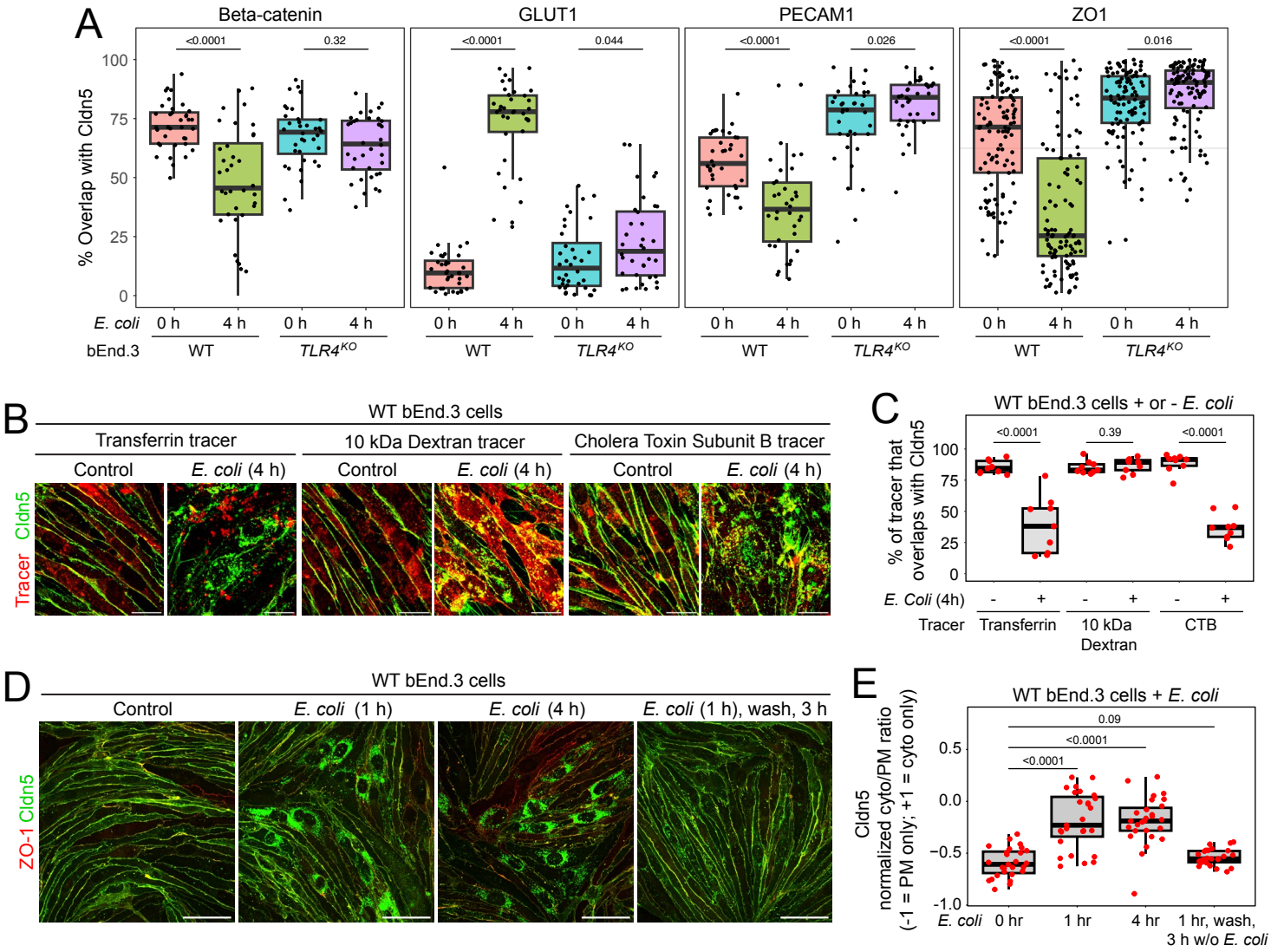

Seegren et al., Figure 5 - figure supplement 1

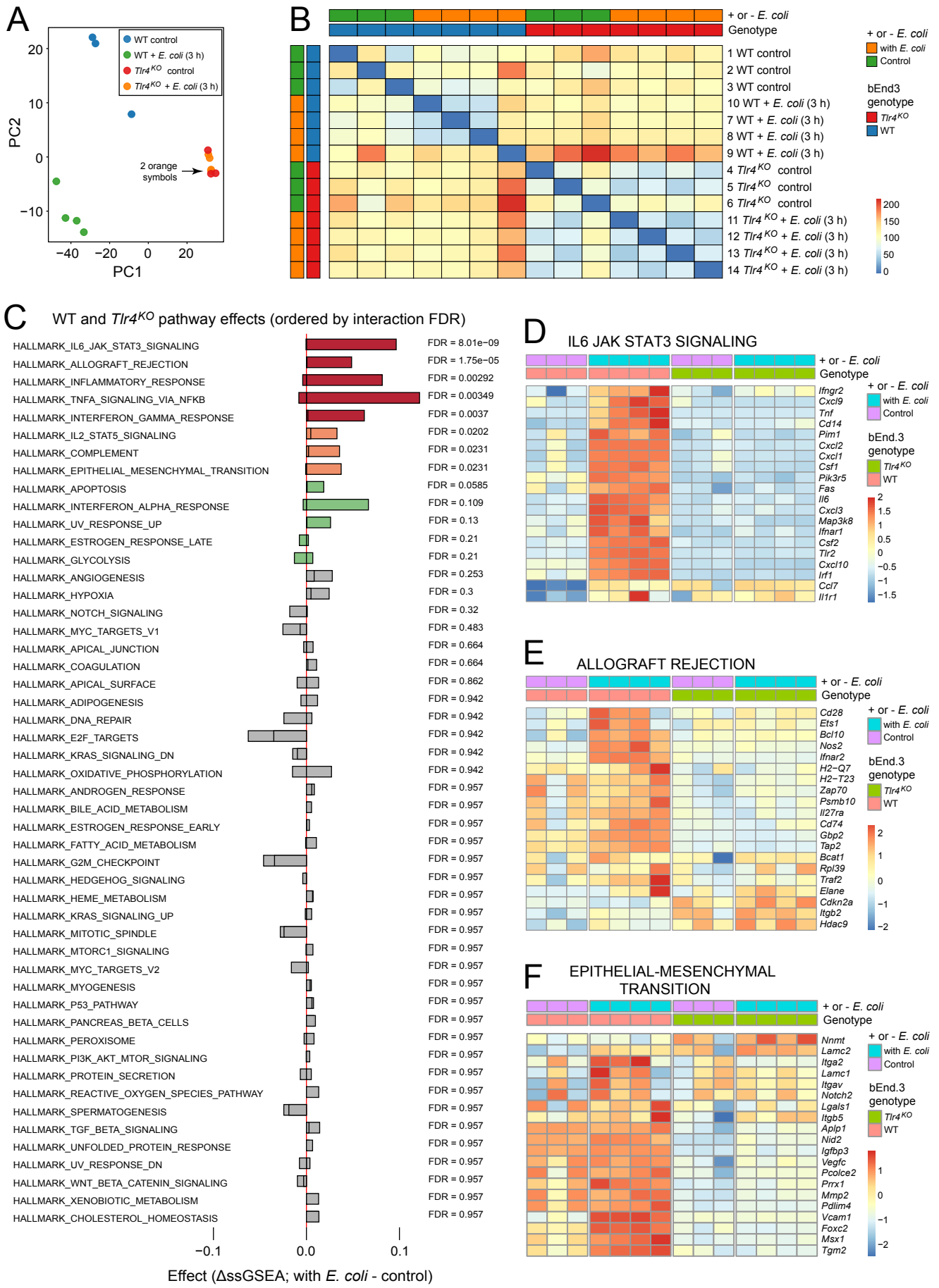

Seegren et al., Figure 6 - figure supplement 1